



## Fracture and wear behavior of high-chromium cast iron obtained from industrial waste and reinforced with alumina particles

Kamil Bochenek<sup>a</sup>, Ivo Dlouhy<sup>b,c</sup>, Witold Węglewski<sup>a</sup>, Marcin Chmielewski<sup>d,e</sup>, Roman Stepanek<sup>c</sup>, Jan Cupera<sup>c</sup>, Katarzyna Pietrzak<sup>a</sup>, Tomasz Chmielewski<sup>f</sup>, Radosław Morek<sup>f</sup>, Michał Basista<sup>a,\*</sup>

<sup>a</sup> Institute of Fundamental Technological Research, Polish Academy of Sciences, 02-106, Warsaw, Poland

<sup>b</sup> Institute of Physics of Materials, Czech Academy of Sciences, 616 00, Brno, Czech Republic

<sup>c</sup> Brno University of Technology, Institute of Materials Science and Engineering, 616 69, Brno, Czech Republic

<sup>d</sup> Lukaszewicz Research Network - Institute of Microelectronics and Photonics, 01-919, Warsaw, Poland

<sup>e</sup> National Center for Nuclear Research, Laboratory of Materials Research, Świerk, 05-400, Otwock, Poland

<sup>f</sup> Warsaw University of Technology, Faculty of Mechanical and Industrial Engineering, 02-524, Warsaw, Poland

### ARTICLE INFO

Handling editor: SN Monteiro

#### Keywords:

High-chromium cast iron  
Iron-alumina composites  
Powder metallurgy  
Fracture  
Wear behavior

### ABSTRACT

In response to the specific requirements of the grinding mill industry, a new composite material for mill crushing parts has been developed. This innovative material, which is both cost-effective and environmentally sustainable, is manufactured from industrial waste of high-chromium cast iron (HCCI) reinforced with aluminum oxide (electrocorundum) particles. The HCCI shavings were crushed, sieved, and milled with the addition of 20 wt% of electrocorundum. The HCCI+20 %Al<sub>2</sub>O<sub>3</sub> powder mixture was consolidated through the process of hot pressing. By optimizing the process conditions, a composite material was obtained with a remarkably high relative density of 99.84 %. Fracture toughness under quasistatic and dynamic loading conditions as well as wear resistance of the HCCI/Al<sub>2</sub>O<sub>3</sub> composite samples, were the main material properties investigated in accordance with the intended application. The wear test program included the ball-on-disc test, the linear abrasive test, and the abrasive blasting test. The base HCCI alloy and the HCCI reinforced with uncoated zirconia toughened alumina were used as reference materials. The results from the Taber linear abrasive test and the abrasive blasting test demonstrated the superior wear resistance of the HCCI/Al<sub>2</sub>O<sub>3</sub> composite over the reference materials. However, in the ball-on-disc test, the HCCI/Al<sub>2</sub>O<sub>3</sub> composite exhibited a higher degree of wear compared to the reference materials. This effect was found to be attributable to a specific microstructure of the reinforcing phase. The HCCI/Al<sub>2</sub>O<sub>3</sub> composite shows promise for industrial applications. However, the hot pressing step requires scaling up to industrial pressing facilities to obtain reasonably sized samples for use in grinding mills.

### 1. Introduction

Grinding mills used in coal-fired power plants, the cement industry, and mineral mining operate under demanding conditions characterized by high abrasive wear and impact from the rigid pieces of the crushed material. One of the persistent industrial problems is the cost of mill maintenance due to the combined effect of abrasive wear and impact damage [1–3]. Also, the effect of wear on the fatigue life of metal components can be significant [4]. Materials typically used for the working parts in the roller and bowl mills include high-chromium alloys [5] and high-chromium white cast iron [6–8]. However, the short

service life of the metal-based parts used in the rolls and bowls has forced mill manufacturers to look for new technological and material solutions. For example, the impact toughness and wear resistance of high-chromium cast iron can be enhanced by laser quenching and laser short peening [9]. A possible remedy for the significant material losses caused by abrasive wear can also be the use of hard ceramic particles to reinforce the metal parts, i.e. iron-matrix composites. In recent years, iron-matrix composites have attracted industrial attention mainly due to their high strength, hardness, and good wear resistance [10]. Wear resistance is not only dependent on hardness, but the interaction between hardness and fracture toughness can also play an important role

\* Corresponding author.

E-mail address: [mbasista@ippt.pan.pl](mailto:mbasista@ippt.pan.pl) (M. Basista).

<https://doi.org/10.1016/j.jmrt.2025.06.109>

Received 30 April 2025; Received in revised form 5 June 2025; Accepted 14 June 2025

Available online 16 June 2025

2238-7854/© 2025 The Authors. Published by Elsevier B.V. This is an open access article under the CC BY license (<http://creativecommons.org/licenses/by/4.0/>).

[11]. In addition, it has been shown that the wear resistance of iron-matrix composites is related to fracture toughness and strength of the ceramic reinforcement [12]. For the application in rolling mills, iron-matrix composites with various ceramic reinforcements are the primary material choice to be explored. Iron and iron-based alloys, such as high-chromium cast iron (HCCI),<sup>1</sup> have been fully characterized in terms of their properties and are commercially available in various types and grades. Tungsten carbide (WC) is often used as a reinforcing phase due to its exceptional hardness and superior wettability with cast iron [13]. However, its high cost can be prohibitive in industrial applications. Therefore, less expensive hard ceramics such as alumina or zirconia-toughened alumina (ZTA) have been used as the reinforcing phase in iron-matrix composites [14–17]. A known drawback of alumina and ZTA particles is their poor wettability by molten iron or its alloys [14]. Poor wettability can negatively affect the bond strength between the iron matrix and the alumina reinforcement. Surface metallization of ZTA particles by mixing with Ti–Ni powder [16] or by electroless plating of Ni [17] has been used to overcome this problem. Other approaches where the interfacial bonding was enhanced by chemical reactions at the interface have been proposed in Refs. [18,19]. Metallurgical bonding was achieved in an infiltration cast ZTA/Fe composite by introducing the Ni–Ti or Ni–Cr transition layers between the ZTA particles and the iron matrix [20,21].

The typical manufacturing routes for iron-matrix MMCs employ pressure casting or infiltration casting processes [15,23]. The infiltration methods require preparations of ceramic preforms [22]. However, the liquid phase fabrication methods of MMCs, such as infiltration casting [15,23], are often accompanied by process induced structural flaws and defects [19]. Moreover, additional technological steps, such as electroless plating of ceramic particles to improve the matrix-reinforcement interfacial bonding, are cumbersome and costly. It should be noted that an HCCI/ZTA composite has also been produced by rapid flow mixing followed by high pressure composing, which does not require particle coating or the use of preforms [24].

One issue that often arises during the manufacture of iron-matrix MMCs through casting is the inhomogeneous dispersion and agglomeration of the reinforcing particles [25,26]. The powder metallurgy route including preparation of homogeneous powder blends by ball milling and consolidation by hot pressing can minimize the particle agglomeration [25]. Recently, the selective laser melting (SLM), a 3D printing technique, has been employed to fabricate particle reinforced iron-matrix composites. The SLM enables a precise manufacture of complex shape components at low cost. However, insufficient interfacial bonding between particles and the matrix is still an issue in SLM produced iron-matrix particulate MMCs [25].

Inspired by the specific requirements of the grinding mill industry, in this paper a new composite material for mill crushing parts is proposed which is both cost-effective and environmentally sustainable. Unlike many research works which utilized coated ZTA particles to reinforce the HCCI matrix [14–19], our composite was manufactured from industrial waste of high-chromium cast iron (HCCI) reinforced with aluminum oxide (electrocorundum) uncoated particles. This HCCI/Al<sub>2</sub>O<sub>3</sub> composite has a very high relative density (99.84 %), enhanced wear resistance in linear and abrasive blasting tests, and fairly good fracture toughness under quasi-static and dynamic loading conditions compared to the base HCCI alloy commonly used by mill manufacturers to repair working parts damage.

A key objective of this work was to achieve the desired material properties while keeping manufacturing costs relatively low. This requirement influenced the choice of starting materials, namely the HCCI from the waste shavings and the alumina powder as electrocorundum, a low-cost ceramic material. This study is novel not only

<sup>1</sup> High-chromium white iron (HCWI) is also used in the literature when the C content is high.

**Table 1**

Elemental composition of the HCCI shavings.

Element	Cr	C	Si	Mn	V	S	Fe
wt%	22.6	5.3	3.3	<1	<0.4	<0.3	rest

because of the innovative material itself, but also because of the processing technology employed. The hot pressing technique used to consolidate the HCCI/Al<sub>2</sub>O<sub>3</sub> composite has several advantages over casting and infiltration methods. These advantages include higher process repeatability, an absence of the liquid phase (which circumvents wettability problems between the iron matrix and alumina reinforcement), and a lower process temperature. Using uncoated electrocorundum particles to produce the HCCI/Al<sub>2</sub>O<sub>3</sub> composite further enhances its cost-effectiveness.

## 2. Materials and methods

The HCCI shavings received from FPM S.A. company (Poland), with the chemical composition presented in Table 1, were used as the matrix material. A milling procedure was adopted to convert the shavings of an average size of 10–20 mm into a ~100 μ powder.

The shavings from a commercial G-X300 type HCCI alloy (according to the DIN1695 standard) were first crushed in a uniaxial hand press in a steel mold and then milled in a planetary ball mill (Fritsch Pulverisette 5) using tungsten carbide balls of 10 mm diameter and the following milling parameters: rotational speed 200 rpm, ball-to-powder weight ratio (BPR) 5:1, total milling time 2h (10-min milling intervals separated by 15-min cooling breaks). The fragmented HCCI shavings were then sieved through a 0.5 mm sieve. In the next step the sieved HCCI powder was milled with 20 wt% of aluminium oxide (electrocorundum EA 1200, supplied by KOS) or 20 wt% of ZTA (75Al<sub>2</sub>O<sub>3</sub>/25ZrO<sub>2</sub>, supplied by GoodFellow Ltd) to obtain the composite powder mixtures. The electrocorundum and ZTA powders in the as-received condition are illustrated by SEM images in Fig. 1. The spherical particles of the as-received ZTA powder shown in Fig. 1b are actually conglomerates that radically change their shape and size after grinding in a planetary ball mill (Fig. 1c). This will have a profound effect on the wear behavior of the HCCI/20ZTA composite as discussed in section 3.2.3.

The milling time to obtain the composite powder was 3h, the rotational speed 200 rpm, and the BPR 5:1. The process of preparing the composite powder from HCCI waste shavings and the commercial electrocorundum powder is schematically depicted in Fig. 2. The same preparation process was used for the HCCI and ZTA powders.

Tungsten carbide (WC) balls with a diameter of 10 mm were used for milling, without any additional milling media, and the process was carried out in air. WC-lined jars were used to ensure durability and consistent energy transfer. The use of an inert atmosphere was intentionally avoided in order to develop a simple, cost-effective, and robust process that does not rely on controlled environments. The high hardness and density of the WC balls and mill interior were essential to generate the high impact energy needed for effective crushing of the HCCI shavings, particularly during the initial stages of milling.

The prepared powder mixtures of HCCI+20 %Al<sub>2</sub>O<sub>3</sub> and HCCI+20 % ZTA were densified in a hot press (Thermal Technologies LLC) at a temperature of 1175 °C in vacuum of 5 × 10<sup>-6</sup> mbar for 60 min dwell time under a pressure of 20 MPa. Finally, discs with a diameter of 48 mm and a thickness of 6 mm were produced. The heating rate was set to 10 °C/min up to the dwell temperature of 1175 °C. The cooling rate was also set to 10 °C/min from the dwell temperature down to 500 °C. Then, the system was allowed to cool freely to room temperature. A pressure of 20 MPa was maintained from the start of the process and released during cooling at 500 °C.

The microstructure of the sintered composite samples prior to fracture testing was examined using light-optical microscopy and scanning electron microscopy (SEM). The microstructure analyses after the

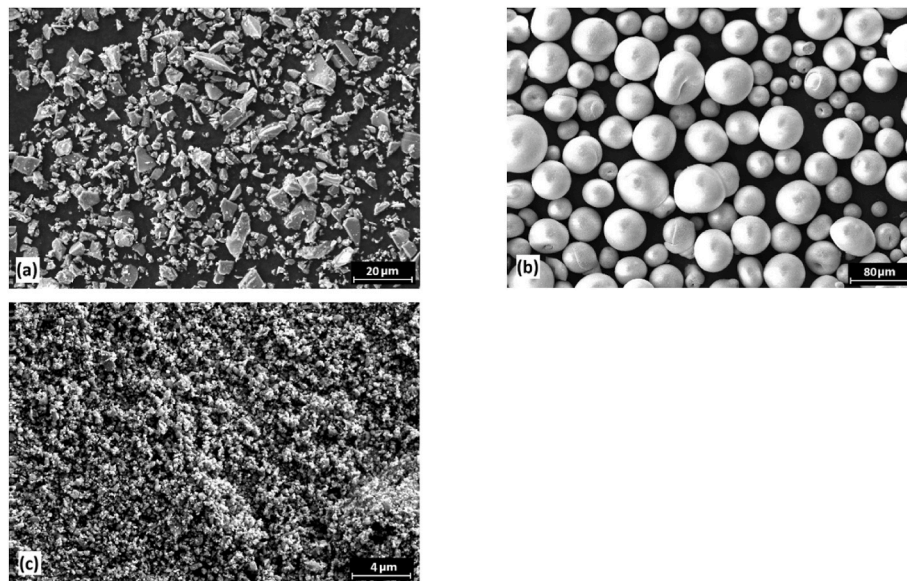


**Fig. 1.** SEM images of the as-received ceramic powders of (a) electrocorundum (average particle size 3.01  $\mu\text{m}$ ), (b) ZTA composed of  $75\text{Al}_2\text{O}_3 + 25\text{ZrO}_2$  (average particle size 45.7  $\mu\text{m}$ ). Fig. 1c shows the effect of milling on the shape and size of ZTA particles (average particle size decreased to 1.42  $\mu\text{m}$ ).

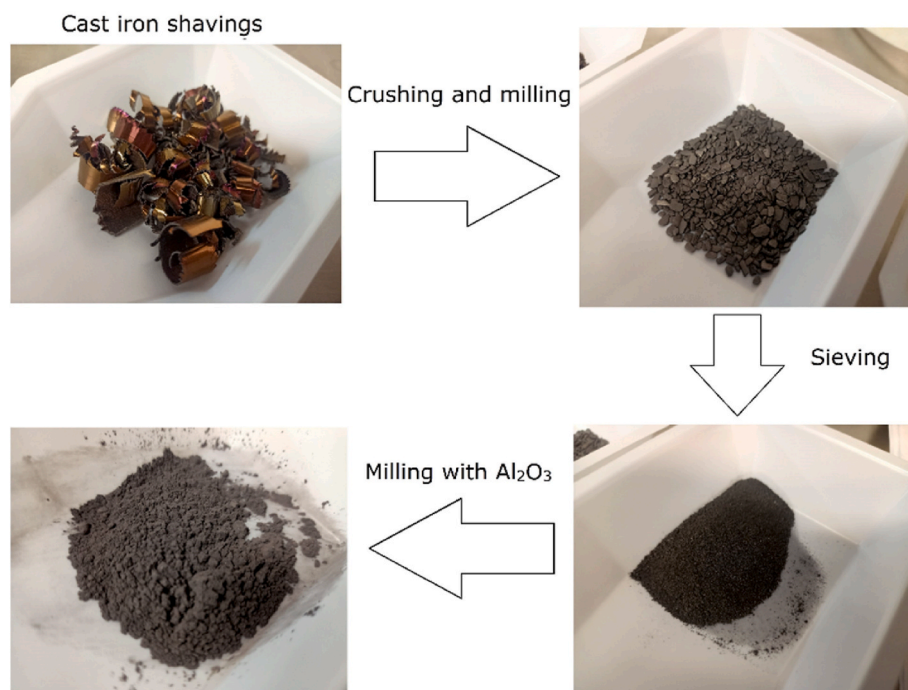


**Fig. 2.** Stages of the preparation process of the powder mixture from the HCCI waste shavings and commercial alumina powder (electrocorundum).

fracture tests were carried out on broken halves of the samples used to determine the fracture toughness. To ensure representativeness of the SEM experiments, they were duplicated by using two samples that were assumed to be identical but one of which had better fracture toughness than the other. The microstructures were evaluated in three orientations, one of which corresponds to the fracture plane of the sample and is referred to as transverse, and the other two in the direction of the longitudinal axis of the samples. Only slight anisotropy was observed and detailed microstructure along with key phase analysis was performed in the transverse orientation.

The light-optical and SEM observations were carried out on metallographic sections of broken samples prepared according to standard methods. The samples were ground with SiC paper and polished with 3

and 1  $\mu\text{m}$  diamond pastes. For the final step, a colloidal silica suspension (Struers OPS) was used to remove damaged surface layers. The evaluation of the microstructure and the hardness measurements were first carried out in the unetched state. After etching, the microstructure was examined using a Zeiss Ultra Plus scanning electron microscope equipped with a Backscattered Electron Imaging (BSEI) detector and an Energy Dispersive Spectroscopy (EDS) detector. Where necessary for phase identification, microstructural analyses were supplemented by EDX microanalyses. X-ray diffraction (XRD) with Philips X'Pert, 40 kV, Co K radiation at  $\lambda = 1.7903 \text{ \AA}$ ,  $2\theta = 30\text{--}120$ ) was performed to evaluate the phase composition.

The  $5 \times 7 \times 38 \text{ mm}^3$  rectangular bars for fracture testing were machined from the sintered HCCI+20 % $\text{Al}_2\text{O}_3$  discs by wire-cutting (Mitsubishi

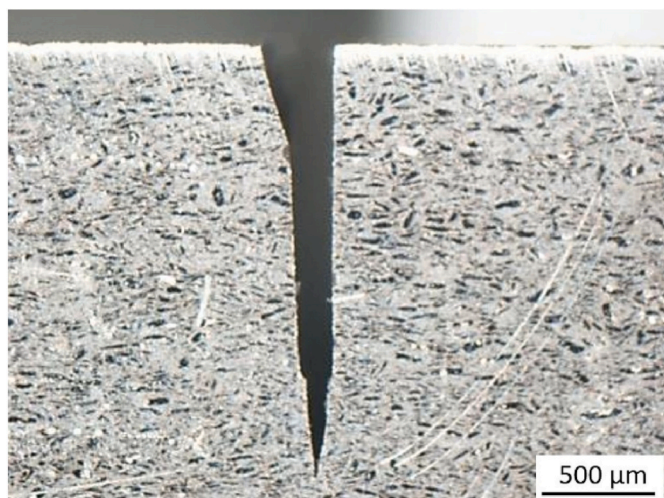


**Fig. 3.** Side view of a notch produced by diamond wheel cutting and razor blade sharpening.

MV1200R). All flat surfaces were ground on a diamond disc using polishing cloths with a diamond suspension of up to  $1\ \mu\text{m}$  (Presi Mecatech 334). The V-notches on SEVNB specimens were prepared using a diamond saw (Buehler ISOMET 5000) and a custom-made notching machine with a razor blade and a diamond paste (9, 6 and  $3\ \mu\text{m}$ ). The total depth of the notch was approximately 2 mm as shown in an illustrative specimen in Fig. 3.

The quasistatic fracture tests were conducted using an Instron 8862 universal testing machine, equipped with a system load cell measuring 100 kN and a more sensitive load cell with a capacity of 5 kN. The fracture toughness ( $K_{IC}$ ) was measured in SEVNB probe according to the ISO 23146 standard [27]. Since the plastic part of the deformation energy was non-negligible, the fracture toughness  $K_{JC}$  was determined according to ISO 12737 standard [28]. Dynamic fracture toughness was determined using a Zwick/Roell B5113.303 machine with a 7.5J hammer and an initial high of  $30^\circ$  (the so-called “low blow method”).

The impact rate was 1 m/s. The tests were designed according to the standard ISO 26843 [29]. At least 5 specimens were prepared for each of the abovementioned tests.

The new composite and reference materials were evaluated for their wear resistance at room temperature using two types of wear tests that represent different contact conditions: the ball-on-disc test (Anton Paar High-Temperature Tribotester) and the linear abrasion test (Taber Linear Abraser 5750) with a flat end pin (Fig. 4a and b). The ball-on-disc test is a commonly used lab test to evaluate the wear properties of materials. In turn, the Taber linear abrasion test with a flat-end pin, where the contact surface area is initially larger than in the ball-on-disc test, is relevant for certain applications, such as grinding mills. The mills manufacturer FPM S.A. prepared a HCCI layer cladded on a steel plate as the reference material for the wear resistance testing. Additionally, the sintered HCCI powder, designated as HCCI (HP) in the following text, was tested for wear resistance. This powder was produced by crushing HCCI shavings and consolidating them using hot pressing. The ball-on-disc tests were performed using a 6 mm diameter sapphire ball under a load of 10 N, rotational speed of 100 rpm, and 120 min of the testing time. This resulted in a total wear track length of 754 mm. The Taber linear abrasion tests were conducted under a load of 20.1 N, at a speed of 60 cycles per minute (back-and-forth stroke arm movements), with a cycle length of 0.0381 m, and a total testing time of 20 h. This resulted in a total wear track length of 1828.8 m. An H-10 type cylindrical wearaser with a 6.35 mm diameter was used as the counter specimen. Prior to the wear tests, the sample surfaces were ground on an EQUITOP ESG-1224TD surface grinder and cleaned in isopropanol. The wear profiles after both tests were measured using Dektak 150 Veeco scanning profilometer.

In addition to the ball-on-disc and Taber linear abrasion tests, the wear resistance was evaluated under abrasive blast using a customized device manufactured by SciTeeX company (Poland) as shown in Fig. 4c and d. The operating conditions of the crushing mills are better represented by the impact abrasive wear tests (e.g., Refs. [1,15,30]) or even three-body abrasive wear tests (e.g., Ref. [31]). However, during the course of this research, access to such specialised experimental setups was limited. Consequently, the available setup depicted in Fig. 4c and d was employed to assess the resistance of the HCCI/ $\text{Al}_2\text{O}_3$  composite to

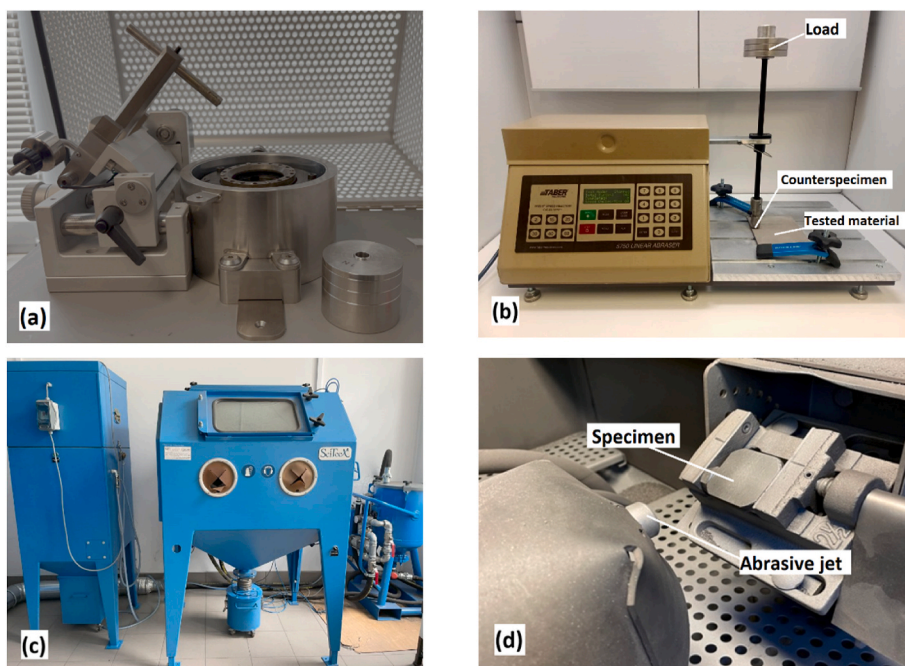


**Fig. 4.** Devices used for wear resistance testing: (a) Anton Paar THT ball-on-disc setup, (b) Taber Linear Abraser 5750 (c) general view of the stand for testing of abrasive blasting resistance, (d) the inside of the working chamber of the setup for abrasive blasting with a sample mounted.

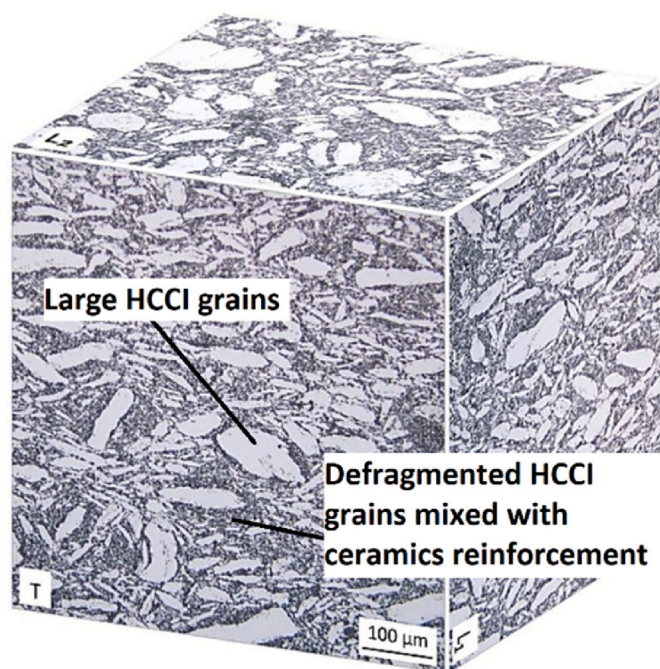


**Fig. 5.** Light-optical micrographs of microstructure of unetched samples (T - transversal, L<sub>1</sub> - longitudinal side, L<sub>2</sub> - longitudinal upper directions; magnification 200×). White areas - HCCI, dark - HCCI matrix/Al<sub>2</sub>O<sub>3</sub>.

abrasive blast and to conduct a comparative analysis with the behavior of the reference materials in this test.

The abrasive blasting resistance tests were carried out using the following parameters: (i) type and granulation of the abrasive - broken steel grit WGH 40 (according to ISO 11124-3) with a hardness of 60-68HRC and a homogeneous martensitic and/or bainitic microstructure, (ii) angle of incidence of the abrasive jet in relation to the sample surface: 30° and 70°; (iii) length of the blasting jet: 700 mm; (iv) diameter of the pneumatic nozzle: 9 mm; (v) air pressure supplied to the

nozzle: 4.3 bar; (vi) duration of the impact of the abrasive jet on the tested surface: 6 cycles, 10 s each. Flat specimens with the in-plane dimensions of approximately 40 mm × 40 mm were prepared for the abrasive blasting tests composed of six cycles. The amount of the worn material was evaluated as a loss of mass weighed with a RADWAG PS 1000.R2 (Poland) electronic balance with an accuracy of 0.001 g.

### 3. Results and discussion

#### 3.1. Microstructure

The light-optical macro-images of the HCCI+20 %Al<sub>2</sub>O<sub>3</sub> composite in three directions T, L<sub>1</sub>, L<sub>2</sub> from unetched metallographic cross sections are shown in Fig. 5. The microstructure is typical of a random but homogeneous distribution of bright areas (hereafter referred to as "white areas") within the darker heterogeneous phase (hereafter referred to as "matrix"). The microscopic images also reflect the slight changes in the orientation of the "white areas" due to the influence of pressure during the consolidation of the composite by hot pressing.

After etching, the metallographic sections (Fig. 6) show that the "white areas" are original HCCI powder particles consisting of large grains (primary/ledeburitic high-chromium carbides) and the granular structure of HCCI. The primary carbides are either unbroken (Fig. 6a) or completely broken into small pieces (Fig. 6c). The darker "matrix" is not a pure HCCI phase, but a heterogeneous mixture of fine HCCI particles and Al<sub>2</sub>O<sub>3</sub> particles (dark, fine grains) formed during mechanical milling (light grains).

The mixture of nanometric HCCI and Al<sub>2</sub>O<sub>3</sub> particles can be seen from the SEM image in Fig. 7. The interfaces between the HCCI and aluminium oxide grains are generally smooth and crack free, except for the parts where mixed nanometric HCCI and Al<sub>2</sub>O<sub>3</sub> particles are located.

Fig. 8 shows similar areas as observed by SEM in secondary electron mode (SE) and in backscattered electron mode (BSE). The microscopic images from SEM are complemented by the mapping of selected elements from EDS (Fig. 9). The elemental mapping clearly reflects the phases present in the composite. There is a very good overlap between the carbon and chromium maps, demonstrating the Cr carbides declared above as primary/ledeburitic carbides. It also shows that iron is present

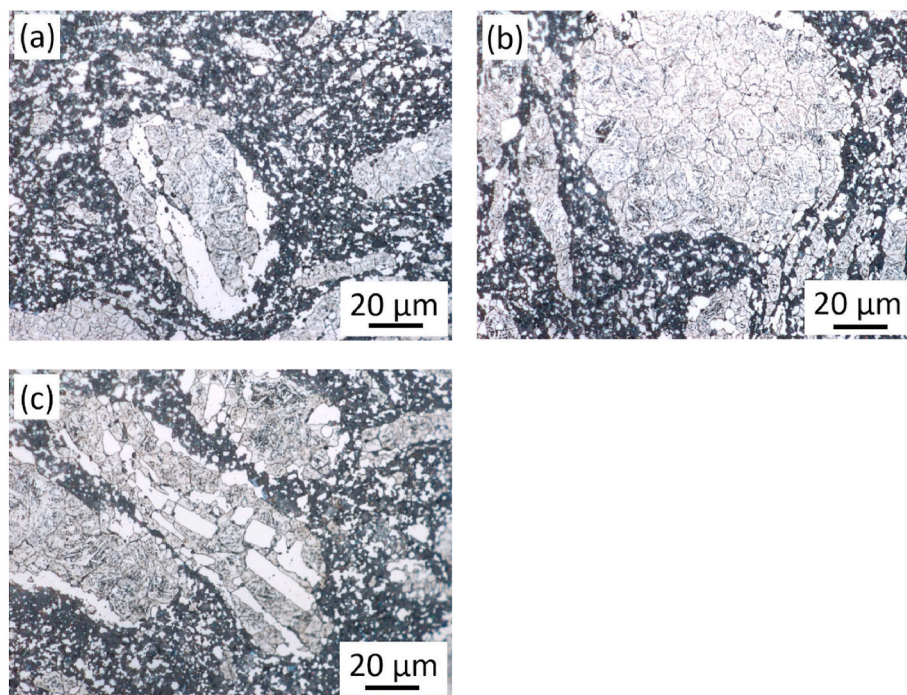


**Fig. 6.** Light-optical microscopy images of etched microstructures in three orientations (a) T, (b) L<sub>1</sub>, and (c) L<sub>2</sub>; magnification 1000×.

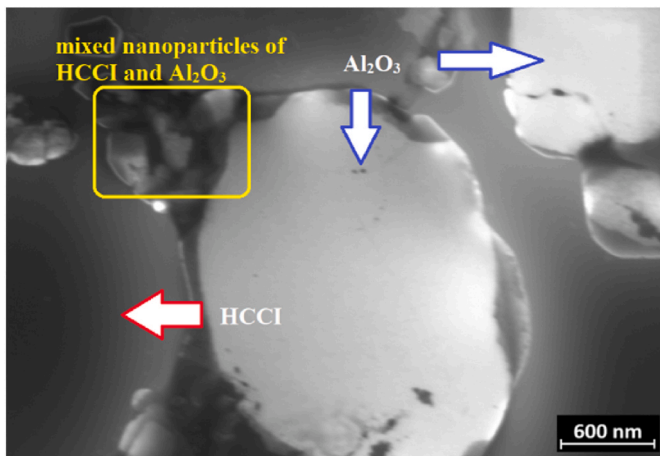


**Fig. 7.** High magnification SEM image showing interfaces between the HCCI and aluminium oxide grains being generally smooth and crack free. However, high-energy ball milling resulted in the formation of mixed nanoparticles of HCCI and  $\text{Al}_2\text{O}_3$  (marked by the yellow rectangle).

in the white areas (and where there are no primary carbides) and in mixture with aluminium. There is also a very good correlation between the presence of aluminium and oxygen, indicating the presence of alumina oxides in locations where both chromium carbides and iron are absent or low. The distribution of other elements in the HCCI was not convincing, except for a few isolated particles containing Si. Since elevated oxygen content was observed at the same location as Si, these particles are likely to be silica inclusions.

Individual areas identified on the element maps were examined in more detail by localized analyses. The results are summarized in **Figs. 10 and 11** and the corresponding **Tables 2 and 3** with the data from EDS. Typical results were selected from a statistically meaningful number of analyses.

Preliminary observations indicate that the larger "white areas" contain two main phases, all typically of the order of  $10\ \mu\text{m}$  or larger in size: Light particles/plates with no internal substructure and a granular structure indicative of a substructure of plate martensite. In the first case, high-chromium carbides were identified. These carbides are in different stages of their fragmentation, from the original unbroken form (referred to as LC - ledeburitic carbides in **Table 2**) to separate more or less equiaxed particles (EC - carbides in **Table 2**) randomly located in the granular HCCI matrix and formed during mechanical alloying. In the second case, no secondary carbides were observed in the HCCI matrix. The composition corresponding to **Fig. 10** can be seen in **Table 2**. Deep etching revealed plate martensite in some locations with the typical zig-zag morphology between the very first plates. In some cases, internal twins are observed, which are typical of plate martensite.

The phases forming the "matrix" of the composite microstructure were quite clearly identified as alumina particles and very fine HCCI grains, see **Fig. 11** and the corresponding compositions in **Table 3**.

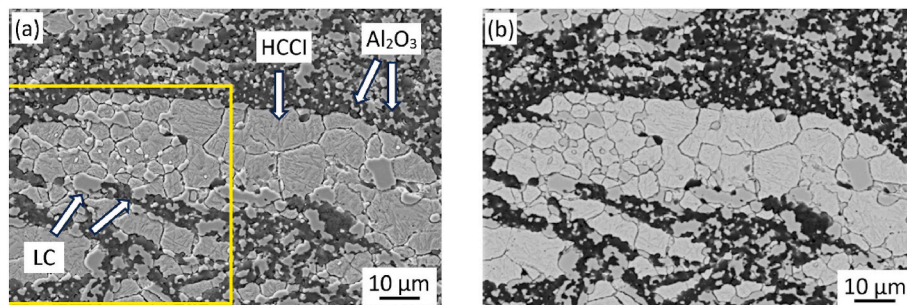


**Fig. 8.** SEM images of etched microstructures of HCCI+20% $\text{Al}_2\text{O}_3$  composite (a) SE, (b) BSE; T, magnification  $1000\times$ .

The composite phases discovered by microstructural observations coupled with EDS analyses were confirmed by XRD analyses. For this purpose, an analysis of HCCI without the reinforcing  $\text{Al}_2\text{O}_3$  phase sintered from the same starting material as the composite samples was also performed. An example of the diffraction spectra is shown in **Fig. 12**.

The quantitative XRD analyses revealed 54.2 wt% of a solid solution formed by a bcc lattice and 12.6 % of a solid solution of iron formed by an fcc lattice for the HCCI reference sample. In addition, ledeburitic carbide of the  $\text{Cr}_7\text{C}_3$  type was clearly identified in an amount of 33.1 %. Repeated analyses of the HCCI/ $\text{Al}_2\text{O}_3$  composite (a total of 3 measurements were performed) revealed 25.5 wt% aluminium oxide phase, 31.4 % primary  $\text{Cr}_7\text{C}_3$  carbides and up to 43.1 % iron solid solution (HCCI matrix). The presence of retained austenite in the composite is difficult to confirm accurately due to the overlap of the dominant austenite peaks with the  $\text{Al}_2\text{O}_3$  peaks. When the austenite model is included in the calculation, its presence is possible up to 5 wt% (for HCCI it was 12.6 wt%).

The reported difference in retained austenite content between the HCCI and the HCCI+20% $\text{Al}_2\text{O}_3$  composite is significant despite the overlap of the main peaks. This fact can be seen from the inserted image with an enlarged detail of the part of the spectrum in the range  $2\theta$  from  $41$  to  $49^\circ$  (**Fig. 12**). The intensity of the (011) peak of martensite (Fe-bcc) at  $2\theta = 44.5^\circ$  is comparable in both spectra (so that the intensities of the other peaks of both records reflect this fact). In the XRD spectrum of the HCCI matrix (without  $\text{Al}_2\text{O}_3$ ), the position (111) of the austenite peak ( $2\theta = 43.5^\circ$ ) is significantly higher than in the peak of the composite, where a clear overlap with the  $\text{Al}_2\text{O}_3$  peak (113) ( $2\theta = 43.3^\circ$ ) can also be seen. With the same austenite content in both samples, the intensity of the (111) austenite peak in the spectrum of the composite should be higher due to the overlap with the  $\text{Al}_2\text{O}_3$  peak (113), but exactly the opposite is the case. This effect cannot be explained well enough by an artefact/distortion of the measured record, but is clearly due to a different state of the structure. Behind the decrease in the amount of retained austenite can be seen, firstly, its decomposition during the mechanical milling/mixing in the production of a matrix containing  $\text{Al}_2\text{O}_3$  particles and, secondly, the temperature used in the compaction process has partly contributed to its destabilization. The retained austenite content can be decisive for the behavior of the composite under contact stress. In general, its optimised content can positively influence both fracture behavior and wear resistance, [32]. The residual austenite contributes to higher fracture toughness due to its ductility and dissipation of deformation energy through transformation-induced martensitic transformation in the process zone of the propagating crack. Although a reduction in the volume fraction of austenite reduces the binding of hard particles in the matrix, a lower volume fraction of retained austenite simultaneously leads to a higher hardness and thus to a higher wear resistance [32,33]. The mechanically induced transformation of retained austenite during wear is considered beneficial in areas where stresses or deformations are localised (mainly in contact). Due to the overlap of the corresponding  $\text{Al}_2\text{O}_3$  and Fe-fcc peaks, the resulting data on the content of the reinforcing  $\text{Al}_2\text{O}_3$  phase can also be influenced, which was not lower than the reported value (25.5 wt%) in

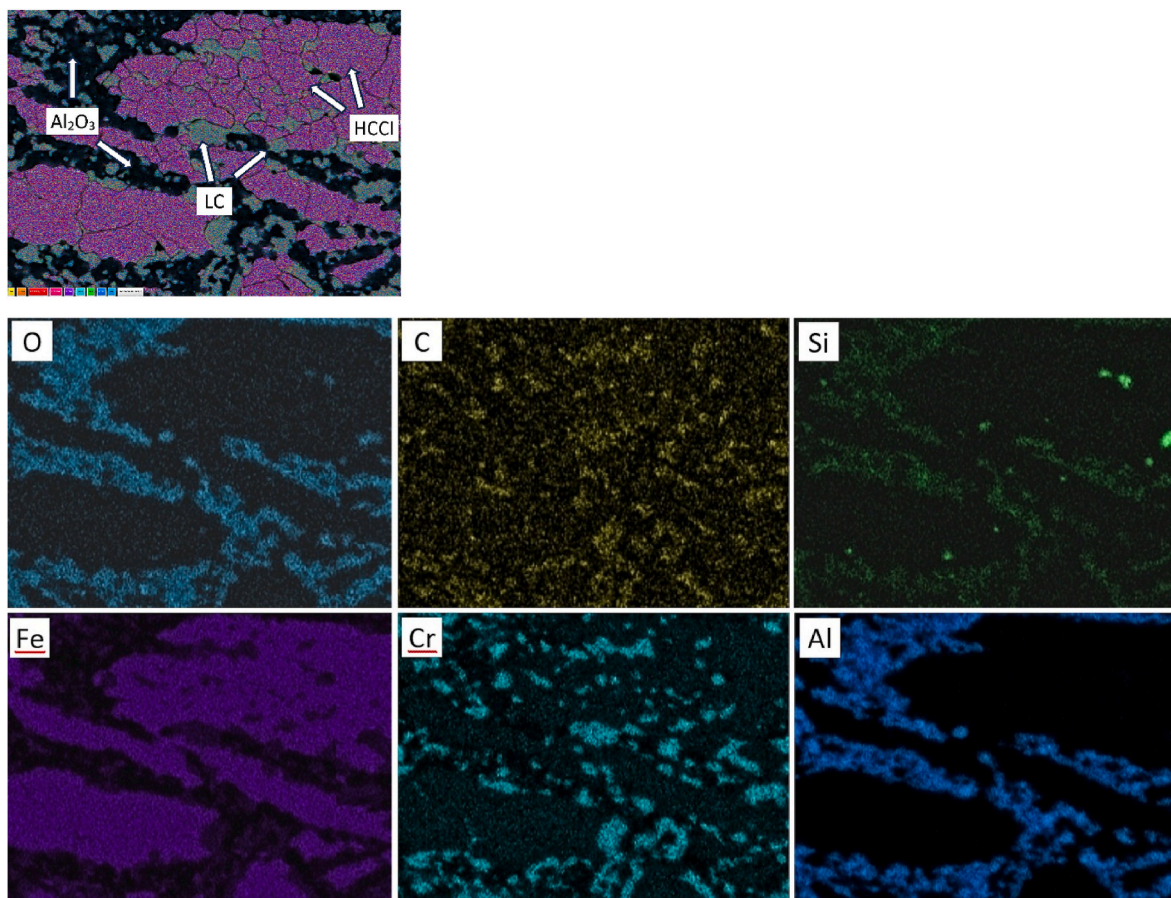


Fig. 9. An overview and EDS maps in selected elements taken from the area highlighted by the rectangle in Fig. 8.

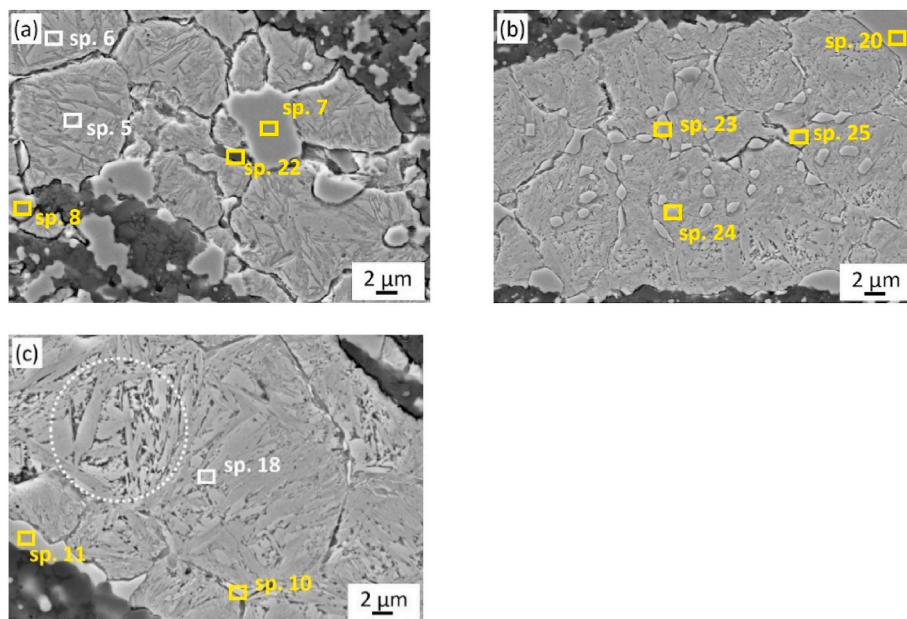


Fig. 10. Localized SEM analyses in selected areas showing locations of EDS microanalysis of carbides and matrix (average values - see Table 2).

all 3 measurements on different samples.

### 3.2. Material properties

#### 3.2.1. Density and hardness

The density of the fabricated composites was evaluated according to the Archimedes law. The densities of the phase materials used in the

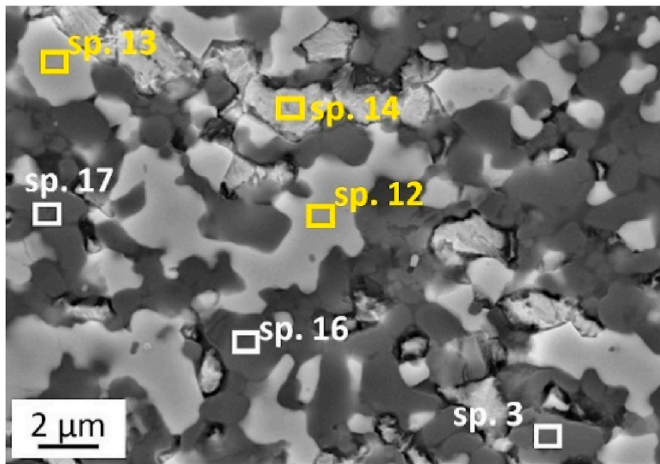


Fig. 11. Details of the selected areas in the matrix areas showing locations of EDS microanalysis of carbides and matrix (average values see Table 3).

Table 2

The local EDS analyses (average values from 3 to 5 locations, in wt%) of locations indicated in Fig. 10 as observed in „white“ areas (HCCI – matrix, LC – ledeburitic carbides, EC – equiaxed carbides).

	Si	V	Cr	Mn	Fe	Ni	Mo
HCCI	0.26 ± 0.09		9.60 ± 0.15	0.36 ± 0.08	87.95 ± 0.37	1.25 ± 0.10	0.70 ± 0.09
LC	0.17 ± 0.01	0.31 ± 0.03	56.77 ± 2.54	0.73 ± 0.10	41.14 ± 2.03		1.49 ± 0.26
EC	0.15 ± 0.03		42.70 ± 0.69		55.11 ± 0.56		1.49 ± 0.30

calculations were: 7.368 g/cm<sup>3</sup> for sintered HCCI, 7.587 g/cm<sup>3</sup> for clad HCCI, 3.921 g/cm<sup>3</sup> for sintered aluminum oxide, and 4.375 g/cm<sup>3</sup> for sintered ZTA. Pure electrocorundum EA 1200 and ZTA were sintered at 1450°C/30 MPa/1h to achieve full consolidation of these materials. The theoretical density of the HCCI+20 %Al<sub>2</sub>O<sub>3</sub> composite, calculated from the densities of the sintered pure phase materials, was 6.27 g/cm<sup>3</sup>. The measured density of the HCCI+20 %Al<sub>2</sub>O<sub>3</sub> composite was 6.26 g/cm<sup>3</sup>, resulting in a relative density of 99.84 %. Such a high relative density of the HCCI+20 %Al<sub>2</sub>O<sub>3</sub> composite is an indication of its high quality due to the precisely tuned process conditions during powder preparation and consolidation by HP. On the other hand, the density of HCCI+20 %ZTA composite consolidated by HP under the same conditions was 6.165 g/cm<sup>3</sup> and the relative density was 95.1 %, indicating a higher porosity of HCCI+20 %ZTA than HCCI+20 %Al<sub>2</sub>O<sub>3</sub>.

The macrohardness was evaluated by the Vickers test (HV1). The average values shown in Table 4 are based on five measurements. The relatively low macrohardness of HCCI+20 %ZTA is related to its lower density than that of HCCI+20 %Al<sub>2</sub>O<sub>3</sub>, as discussed above.

The detailed hardness studies, including macrohardness (HV1) and microhardness (HV0.1) tests, were performed on the hot-pressed HCCI+20 %Al<sub>2</sub>O<sub>3</sub> specimens. The macro and micro hardness of the matrix and "white areas" were evaluated in three orientations (Table 5) of the metallographic section. The differences in the different orientations are not large. On the other hand, the large scatter reflects the heterogeneous structure of the "white areas" (ledeburitic high-chromium

Table 3

The local EDS analyses (average values from 3 to 5 locations, in wt%) of typical phases observed in the „darker matrix“ of Fig. 11 (HCCI – matrix, Al<sub>2</sub>O<sub>3</sub>).

	O	Al	Si	V	Cr	Mn	Fe	Mo
HCCI		1.56 ± 0.69	0.20 ± 0.10	0.29 ± 0.03	54.05 ± 0.49		41.78 ± 0.91	2.29 ± 0.34
Al <sub>2</sub> O <sub>3</sub>	41.29 ± 1.41	47.47 ± 1.32	1.03 ± 0.82		4.23 ± 1.15	0.32 ± 0.17	5.58 ± 1.18	

carbides and HCCI matrix), which vary from case to case depending on the content and fragmentation stage of the LC.

The microhardness values show that there is a significant difference between the white spots and the "matrix" (i.e. the mixture of HCCI and alumina particles). The "white areas" are influenced by the presence of ledeburitic high-chromium carbides, which show an average value of 1227 HV0.1, but at the same time a rather high standard deviation (155). On the other hand, the standard deviation of the "matrix" shows that the distribution of alumina and HCCI particles is quite homogeneous (769 ± 21 HV0.1). It should be noted from the data in Table 5 that the uniaxial hot pressing technique provides a homogeneous hardness distribution along three directions.

### 3.2.2. Fracture toughness

The fracture behavior of the HCCI+20 %Al<sub>2</sub>O<sub>3</sub> composite was one of the two key properties addressed in this study, the other being wear resistance. As mentioned before, the fracture testing was performed

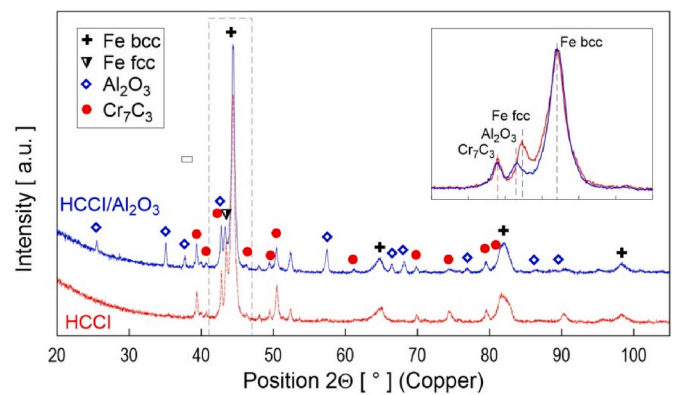


Fig. 12. XRD analysis of phase composition of the HCCI/Al<sub>2</sub>O<sub>3</sub> composite (upper blue spectrum) and HCCI without reinforcement (lower red spectrum). Insert: a detail of the peak identification in position 2θ = 41–49°.

Table 4

Evaluation of macrohardness (HV1) of all investigated materials: HCCI clad HCCI (HP), HCCI+20 %Al<sub>2</sub>O<sub>3</sub> composite, and HCCI+20 %ZTA composite.

	HCCI clad HCCI	HCCI (HP)	HCCI+20 % Al <sub>2</sub> O <sub>3</sub>	HCCI+20 % ZTA
HV1 (macro)	821.11 ± 46.0	798.88 ± 44.0	989.1 ± 24.9	815.8 ± 42.9

Table 5

Evaluation of macro (HV1) and microhardness (HV0.1) of HCCI+20 %Al<sub>2</sub>O<sub>3</sub> composite in three directions as indicated in Fig. 5.

HCCI+20 % Al <sub>2</sub> O <sub>3</sub>	T	L <sub>1</sub>	L <sub>2</sub>	Average
HV1 (macro)	975.3 ± 49.4	991.0 ± 135.7	963.3 ± 15.3	989.1 ± 24.9
HV0.1 (matrix)	749.7 ± 39.8	765.7 ± 22.0	791.0 ± 17.3	768.8 ± 20.8
HV0.1 (white areas)	1247.3 ± 130.7	1234.7 ± 121.6	1199.3 ± 213.9	1227.1 ± 155.4

**Table 6**

Fracture toughness of HCCI+20 %Al<sub>2</sub>O<sub>3</sub> composite and unreinforced HCCI (HP) sintered material from the quasistatic three-point bending test on notched specimens (SEVNB).

Specimen no.	B [mm]	W [mm]	a <sub>0</sub> [mm]	F <sub>5</sub> [kN]	F <sub>C</sub> [kN]	K <sub>IC</sub> [MPa m <sup>1/2</sup> ]	K <sub>JC</sub> [MPa m <sup>1/2</sup> ]
4 (HCCI+20Al <sub>2</sub> O <sub>3</sub> )	5.042	7.055	1.998	1.035	1.042	14.1	16.3
6 (HCCI+20Al <sub>2</sub> O <sub>3</sub> )	5.154	7.028	1.984	1.088	1.088	14.4	16.8
1 (HCCI (HP))	4.913	7.004	2.015	1.115	1.206	16.0	21.8
2 (HCCI (HP))	4.915	7.003	1.955	1.375	1.391	19.3	22.3
3 (HCCI (HP))	4.910	7.012	2.040	1.218	1.275	17.5	22.1
4 (HCCI (HP))	4.916	7.008	1.925	1.201	1.298	16.6	23.5
5 (HCCI (HP))	4.917	7.008	1.945	1.412	1.421	19.7	22.6

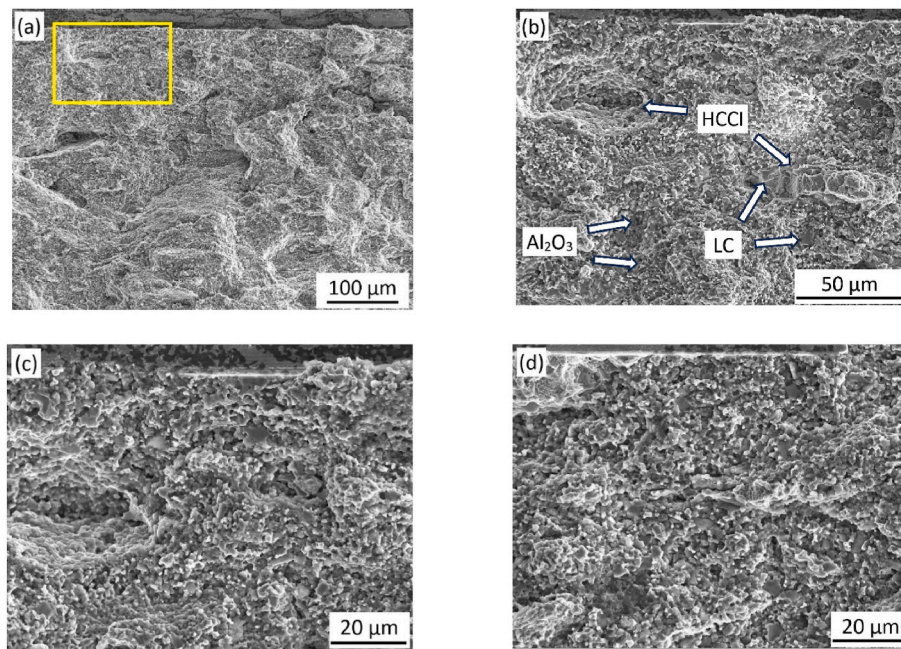


**Fig. 13.** Fracture surfaces of the HCCI+20 %Al<sub>2</sub>O<sub>3</sub> notched specimens broken under quasistatic three-point bending: (a) macro view; (b), (c) details of the area marked by the yellow rectangle, (d) matrix fracture.

under (i) quasistatic conditions, and (ii) impact loading using a 50 J instrumented impact pendulum with 7.5 J hammer. The quasistatic tests were conducted in three-point bending using 100 kN and 5 kN load cells. Some small differences were found in the load measurements obtained from the two load cells. This is a normal consequence of the different stiffness of the load cells. Due to the high porosity of the HCCI+20 %ZTA composite, this section focuses primarily on the fracture behavior of the studied composite HCCI+20 %Al<sub>2</sub>O<sub>3</sub> and the sintered HCCI (HP) material.

#### (i) Quasistatic tests

A standard procedure according to EN ISO 12737 [27] was used to determine the fracture toughness. As a certain plastic/quasi-plastic behavior of the material was observed, the plastic part of the deformation energy was found not to be negligible. This was a reason to include the plastic work in the fracture toughness determination. Both the linear elastic fracture toughness  $K_{IC}$  and the elastic-plastic fracture toughness  $K_{JC}$  were determined. The details of the  $K_{IC}$  and  $K_{JC}$  evaluation are provided in Appendix 1.

The results of the quasistatic tests for the  $K_{IC}$  and  $K_{JC}$  are shown in Table 6 (specimens 4 and 6). The elastic constants  $E$  and  $\nu$  were estimated to be 210 GPa and 0.3, respectively. Both the linear elastic and elastic-plastic fracture toughness values were found to be valid. The average  $K_{JC}$  for HCCI/20Al<sub>2</sub>O<sub>3</sub>, obtained from two repetitions of the SEVNB test in three-point bending is  $16.6 \pm 0.3$  MPa m<sup>1/2</sup>. Fracture

toughness was also measured on unreinforced HCCI (HP) samples prepared from waste shavings under the same process conditions as the HCCI/20Al<sub>2</sub>O<sub>3</sub> composite. The elastic constant  $E$  was estimated to be 199 GPa [34]. The average  $K_{JC}$  values of unreinforced HCCI (HP) specimens from five test repetitions in three-point bending (specimens 1 to 5) is  $22.5 \pm 0.5$  MPa m<sup>1/2</sup>.

The data in Table 6 show that the fracture toughness of the unreinforced HCCI (HP) material is higher than that of the HCCI+20 %Al<sub>2</sub>O<sub>3</sub> composite. A similar observation has been reported for the HCCI alloy matrix in squeeze cast HCCI/ZTA composite [15] and Ti alloy matrix composite [35]. This is related to the microstructure and fracture mechanisms of the materials under investigation. The fracture surfaces of the composite specimens broken during the fracture toughness tests (Fig. 13) show similar characteristics to the original microstructures (Figs. 10 and 11). There are distinct areas that correspond to the "white areas" in the microstructure. These areas serve as weak points in the fracture surface, mainly the interfaces between these areas (HCCI with LCs) and the matrix (fine HCCI with alumina) support steps formation and contribute to a higher roughness of the fracture surface. Under these conditions, the fracture surfaces of these domains are covered with dimples, indicating a ductile mechanism of microvoid coalescence. The fracture of the ledeburitic carbides in the HCCI granular matrix ("white areas") is purely cleavage. The "matrix" surrounding these white areas (consisting of fine HCCI particles and alumina particles) shows no transgranular micromechanism and the fracture morphology can be characterized as typical of very fine-grained/nanocrystalline

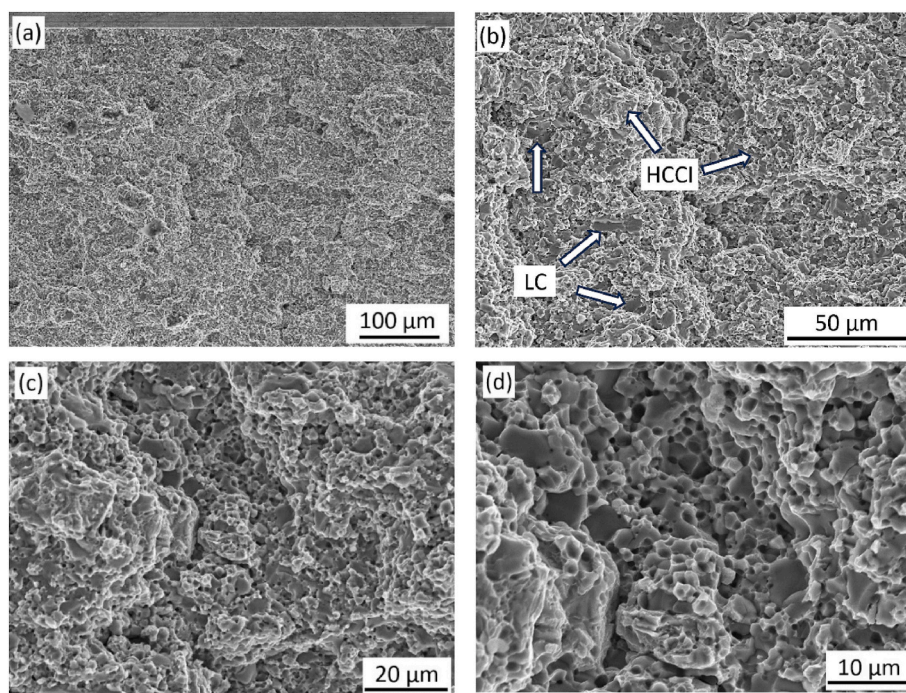


**Fig. 14.** SEM images of the fracture surface of an unreinforced HCCI (HP) specimen after a quasistatic SEVNB test under three-point bending at various magnifications: (a) 500 $\times$ , (b) 1500 $\times$ , (c) 2500 $\times$ , (d) 5000 $\times$ .

**Table 7**

Results of the dynamic fracture test on HCCI/20Al<sub>2</sub>O<sub>3</sub> notched specimens in three-point bending using an instrumented impact pendulum.

Specimen no.	<i>B</i> [mm]	<i>W</i> [mm]	<i>a</i> <sub>0</sub> [mm]	<i>F</i> <sub>Qd</sub> <sup>a</sup> [kN]	<i>K</i> <sub>ICd</sub> [MPa <sup>1/2</sup> ]
5	5.059	7.059	1.969	1.102	14.8
11	5.048	7.025	1.969	1.183	16.1
3	5.034	7.017	1.941	1.151	15.6
7	5.036	7.044	2.008	0.916	12.6
9	5.042	7.021	2.002	1.011	14.0
10	5.056	7.041	1.988	0.861	11.7
12	5.153	7.014	1.988	0.888	12.0

<sup>a</sup> Original data determined from the load-deflection curves shown in Supplementary Material (Fig. A1) as the actual onset of unstable fracture (deviating from regular peak shape).

microstructures with predominantly intergranular decohesion.

From the energetic point of view of energy consumption for crack propagation, the high fracture surface relief (controlled by the "white areas") and the ductile microvoid mechanism in the HCCI matrix of the "white areas" seems to be decisive, while the "matrix" (alumina and fine HCCI grains) contributed only through the intergranular shielding mechanisms and surface roughness.

Fracture surface of an HCCI (HP) specimen without a reinforcing phase after quasistatic loading (Fig. 14a–d) is not as relief as HCCI+20 % Al<sub>2</sub>O<sub>3</sub> composite material broken under similar loading conditions. In this case, the fracture is also controlled by a brittle ledeburitic carbide phase, which manifests itself at the fracture surfaces through larger cleavage facets mainly (Fig. 14d). By interconnecting these sites together, the cleavage facets of the larger ledeburite carbides control the depth of the relief. The areas between these facets are covered with a mixture of mostly fine, relatively shallow dimples, areas of quasi cleavage and cleavage facets of similar size (less than 1  $\mu$ m). The energy dissipation associated with the formation of fine dimples then represents the greatest contribution to the consumption of deformation energy and the fracture toughness achieved.

#### (ii) Impact tests

The tests were designed according to ISO 26843 [29]. The details of the dynamic fracture experiments are presented in Appendix 2. The results of *K*<sub>ICd</sub> measurements for notched HCCI+20 %Al<sub>2</sub>O<sub>3</sub> specimens are given in Table 7, whereas SEM images of the fracture surface are shown in Fig. 15.

From the data in Tables 6 and 7, the average dynamic fracture toughness of HCCI+20 %Al<sub>2</sub>O<sub>3</sub> (*K*<sub>ICd</sub> = 13.8  $\pm$  1.5 MPa m<sup>1/2</sup>) is slightly lower than the average quasistatic fracture toughness (*K*<sub>IC</sub> = 14.3  $\pm$  0.3, *K*<sub>JC</sub> = 16.8  $\pm$  0.3 MPa m<sup>1/2</sup>). This difference must be associated with the fracture mechanism (Fig. 15). The introduction of the reinforcing Al<sub>2</sub>O<sub>3</sub> phase changes the deformation response of the HCCI matrix in the macroscopically dark part of the HCCI+20 %Al<sub>2</sub>O<sub>3</sub> structure, which leads to highlighting the role of larger ledeburite carbides, observed only in the light part of the structure. This is reflected in the higher relief of the fracture surface observed in both quasistatically and dynamically strained test specimens, approximately to the same extent. Although it is a brittle phase, it paradoxically contributes to hardening, in that it represents defect sites in which microcracks form in front of the main crack and the fracture itself is created by connecting these defect sites. At the same time, they are not in the plane of crack propagation, but "zig zag" at certain and varying distances from this plane. This leads to an increase in the area of the real crack, while a local shear stress field is created between the defect spots, which facilitates the formation of cavities manifested in the fracture surface by fine dimples. In essence, this is a toughening process used for brittle non-deformable materials, where the "shear ligament toughening" effect is achieved by controlled defectivity in front of the crack front. This mechanism contributes to the relatively small embrittlement of HCCI+20 %Al<sub>2</sub>O<sub>3</sub> compared to unreinforced HCCI, which would otherwise be induced by introducing a 20 % Al<sub>2</sub>O<sub>3</sub> phase. An order of magnitude higher loading speed shortens the time for the necessary deformation processes, both in relation to the splitting of ledeburitic carbides (controlled not only by the critical fracture stress for their fracture, but also by a certain level of deformation), and also in relation to the deformation required to create a fracture failure when joining defective sites on ledeburite carbides.

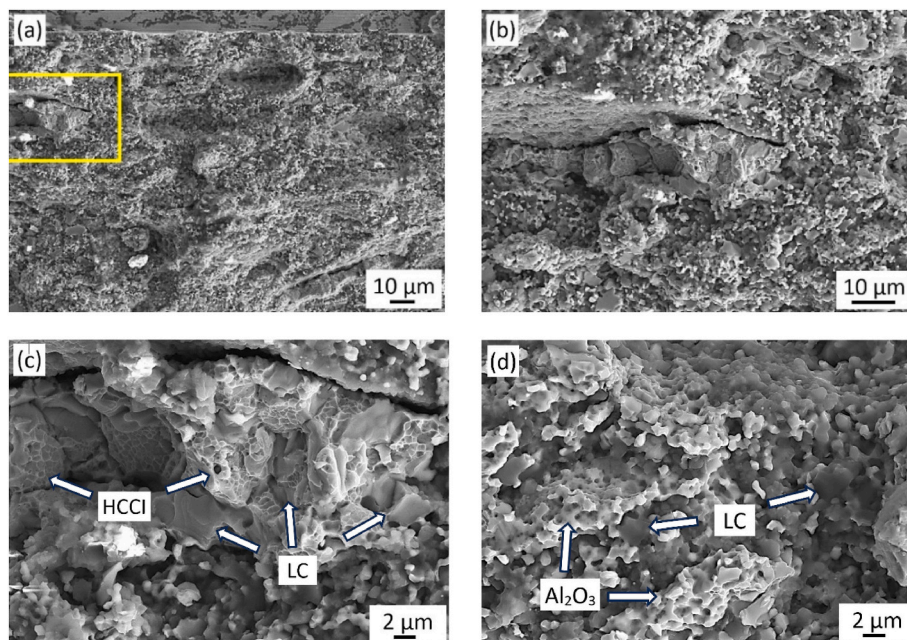


Fig. 15. SEM images of fracture surface of an HCCI+20 %Al<sub>2</sub>O<sub>3</sub> specimen after impact loading at various magnifications to show characteristic features of the dynamic fracture.

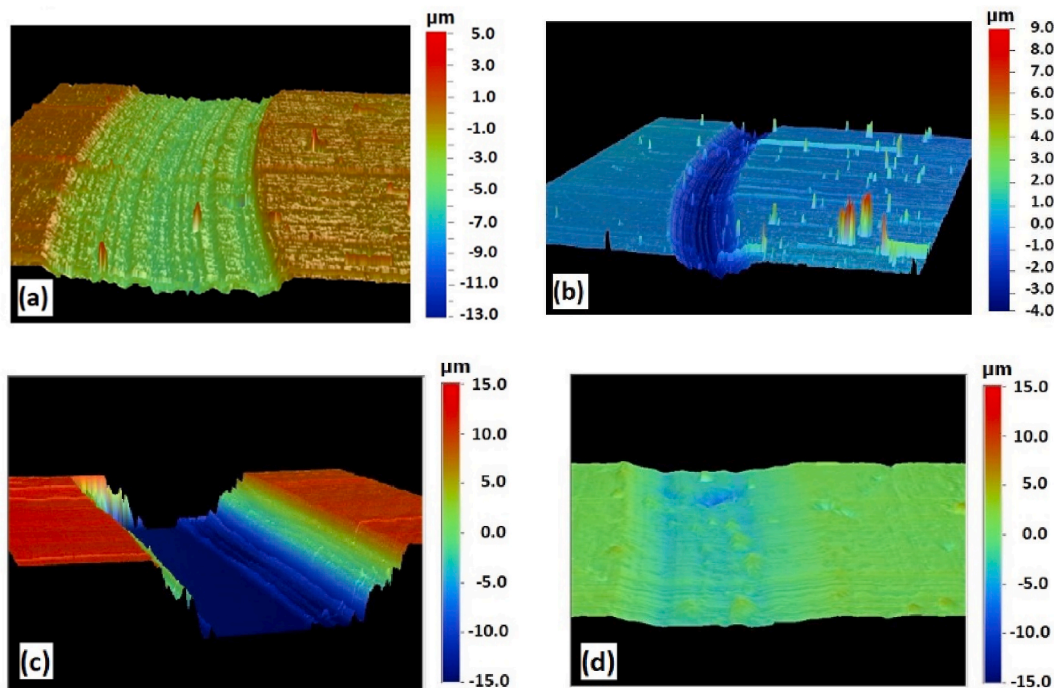


Fig. 16. Wear profiles and the specific wear rates (SWR) after the ball-on-disc test (a) HCCI clad, (b) HCCI (HP), (c) HCCI+20 %Al<sub>2</sub>O<sub>3</sub>, (d) HCCI+20 %ZTA.

Table 8

Specific wear rates (SWR) and the coefficients of friction (CoF) obtained from the ball-on-disc test for HCCI clad, HCCI (HP), HCCI+20 %Al<sub>2</sub>O<sub>3</sub>, and HCCI+20 %ZTA.

Material	SWR (mm <sup>3</sup> /Nm)	CoF
HCCI clad	$2.50 \times 10^{-5}$	0.601
HCCI (HP)	$1.55 \times 10^{-6}$	0.521
HCCI+20 %Al <sub>2</sub> O <sub>3</sub>	$5.25 \times 10^{-5}$	0.736
HCCI+20 %ZTA	$6.10 \times 10^{-6}$	0.563

### 3.2.3. Wear resistance

As already stated, the wear resistance of the HCCI+20 %Al<sub>2</sub>O<sub>3</sub> composite is the key material property from the point of view of its intended use in crushing mills. The specific wear rates of the HCCI+20 % Al<sub>2</sub>O<sub>3</sub> composite and the reference materials were evaluated using three tribological/abrasive wear tests: (i) the ball-on-disc test, (ii) the linear abrasion test, and (iii) the abrasive blasting wear test. In addition, the coefficients of friction were also determined from the ball-on-disc test for the studied materials.

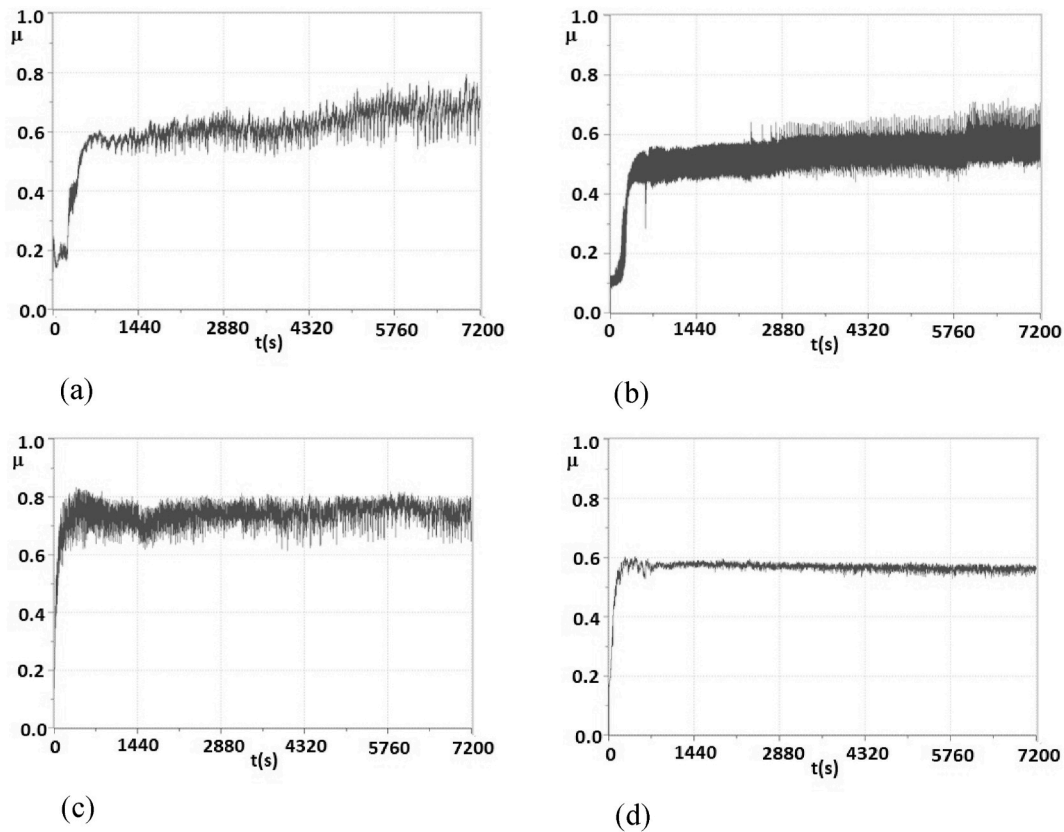


Fig. 17. Coefficients of friction vs. time obtained from the ball-on-disc test for: (a) HCCI clad, (b) HCCI (HP), (c) HCCI+20 %Al<sub>2</sub>O<sub>3</sub>, (d) HCCI+20 %ZTA.

**3.2.3.1. Ball-on-disc test.** The wear profiles after the ball-on disc tests for the materials tested are presented in Fig. 16. The specific wear rates (SWR) and the coefficients of friction (CoF) are given in Table 8. The values of the SWR are the average values taken from the three test runs.

It is evident from Table 8 that the HCCI+20 %Al<sub>2</sub>O<sub>3</sub> composite shows a lower wear resistance (higher SWR) as compared to the other tested materials. The point contact between the composite surface and the sapphire ball in the ball-on-disc test creates high pressure in the early stages of the wear test. This results in tearing off the ceramics particles, which can increase the SWR and the CoF. Fig. 17a–d shows the coefficients of friction vs. time for the HCCI+20 %Al<sub>2</sub>O<sub>3</sub> composite and the reference materials (HCCI clad and HCCI+20 %ZTA). The HCCI clad and HCCI+20 %ZTA exhibit lower coefficients of friction than the HCCI+20 %Al<sub>2</sub>O<sub>3</sub> composite. The highest CoF for the HCCI+20 %Al<sub>2</sub>O<sub>3</sub> composite correlates with the highest SWR value for this material (Table 8). A similar experimental observation can be found elsewhere [36].

It is noticeable that the wear behaviors of the HCCI+20 %Al<sub>2</sub>O<sub>3</sub> and HCCI+20 %ZTA composites in the ball-on-disc test are not proportional

to their hardness (see Table 4), [37]. The HCCI+20 %Al<sub>2</sub>O<sub>3</sub> composite demonstrates superior hardness, yet it exhibits a lower SWR and a higher CoF compared to the HCCI+20 %ZTA composite (refer to Table 8 and Fig. 17c). It is evident that a more in-depth analysis of the inferior wear performance of the HCCI+20 %Al<sub>2</sub>O<sub>3</sub> composite in the ball-on-disc test is needed. The lower wear resistance of the HCCI+20 %Al<sub>2</sub>O<sub>3</sub> composite and its higher CoF are primarily due to the microscopic characteristics of the reinforcing phase, particularly the particle size and morphology. According to Bembalge et al. [38] the coefficient of friction decreases as the particle size decreases from coarse to micro to nano. Fig. 18 shows the SEM images of the HCCI+20 %Al<sub>2</sub>O<sub>3</sub> and HCCI+20 %ZTA composites with the close-up of the reinforcement phases as insets, illustrating their complex internal microstructure. The reinforcing phase in HCCI+20 %Al<sub>2</sub>O<sub>3</sub> (Fig. 18a) consists of micrometric grains, whereas in HCCI+20 %ZTA (Fig. 18b) it has a nanometric structure. During the ball-on-disc test, the micrometric Al<sub>2</sub>O<sub>3</sub> grains are pulled out from the HCCI matrix surface. These grains act as a third body, resulting in the enhanced CoF of HCCI+20 %Al<sub>2</sub>O<sub>3</sub> (Fig. 17c). Joshi et al. [39] have reported a similar effect for micrometric yttrium oxide-reinforced

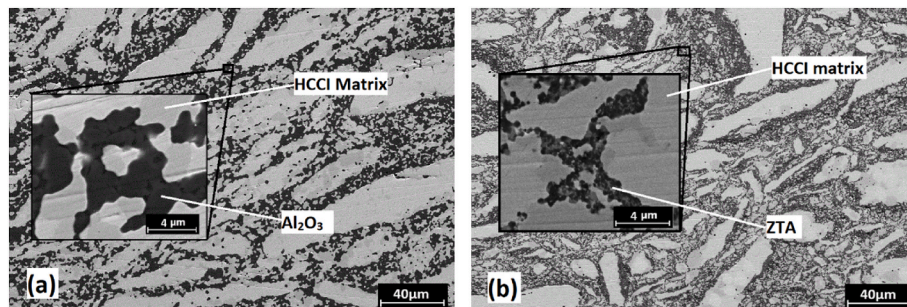
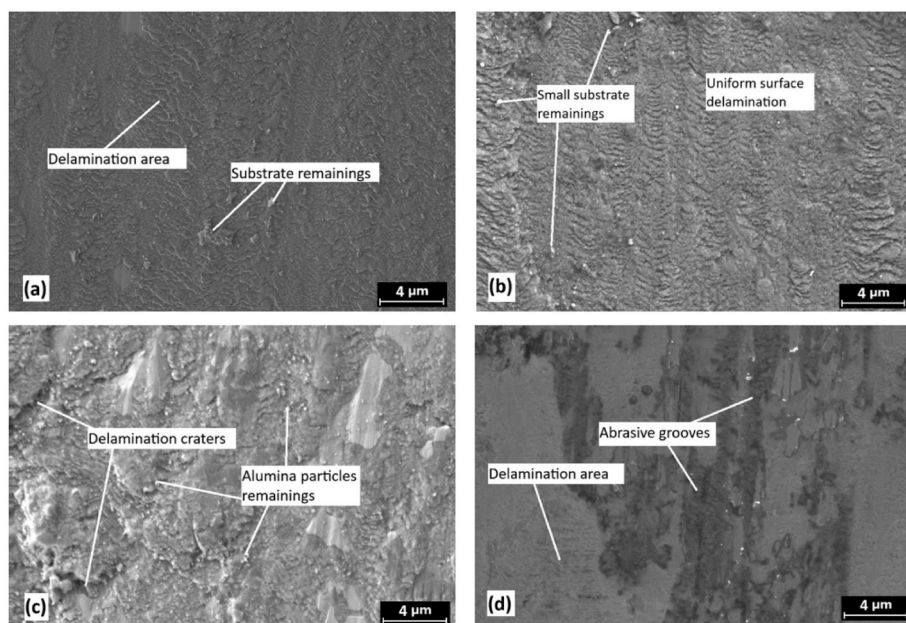


Fig. 18. SEM images of the composites microstructure with close-up view of the reinforcing alumina phases (a) HCCI+20 %Al<sub>2</sub>O<sub>3</sub>, (b) HCCI+20 %ZTA.



**Fig. 19.** SEM micrographs of worn surfaces after the ball-on-disc test: (a) HCCI clad, (b) HCCI (HP), (c) HCCI+20 %Al<sub>2</sub>O<sub>3</sub> composite, (d) HCCI+20 %ZTA composite.

AA-7075 matrix composites. According to that study, increasing the load to 20 kN during pin-on-disc tests resulted in material pulling out from the sample surface. This material acted as an abrasive powder, leading to a higher CoF. In contrast, the lower CoF of the HCCI+20 %ZTA composite (Fig. 17d) is attributed to the presence of ZTA nanograins. These grains act as the rolling media between two mating surfaces, thereby reducing the CoF [35].

Fig. 19 shows the SEM images of the worn surfaces after the ball-on-disc test. The difference in wear behavior of the HCCI+20 %Al<sub>2</sub>O<sub>3</sub> and HCCI+20 %ZTA composites is visually evident in Fig. 19c and d. The HCCI+20 %Al<sub>2</sub>O<sub>3</sub> surface appears rough and riddled with loosely bound particles, while the HCCI+20 %ZTA surface is much smoother and shows less wear. The frictional heating generated during the ball-on-disc test is initially higher because the debris between the pin and the specimen surface is sharper and more abrasive. However, as the test progresses, the slippery action increases, and the heating decreases. This phenomenon leads to the softening of the sample surface, thereby increasing its vulnerability to penetration by the debris material [40]. This process can result in delamination, as illustrated in Fig. 19c and d.

The results of the ball-on-disc test were unfavorable for the HCCI+20 %Al<sub>2</sub>O<sub>3</sub> composite as a material for the working parts in roller and bowl mills. However, the Taber linear abrasive wear test, the results of which will be presented in the following section, seems more representative than the ball-on-disc test for the intended application. This is due to the larger contact surface area between the test specimen and the counter specimen, which is closer to real service conditions.

**3.2.3.2. Taber linear abrasion test.** Abrasion tests using the Taber linear abraser have revealed markedly different wear behaviors of the investigated materials than the ball-on-disc tests. The wear profiles after the Taber test were analyzed using a 3D scanning profilometer (Dektak). The loss of material volume was evaluated by means of the Vision software. The average values of the specific wear rate (SWR) from five repetitions for each of the three materials tested are shown in Table 9. The SWR data in Table 9 indicate an order of magnitude lower abrasive wear of the sintered HCCI+20 %Al<sub>2</sub>O<sub>3</sub> composite than the reference materials HCCI clad, HCCI (HP), and HCCI+20 %ZTA (uncoated). The present experimental findings are at variance with the ball-on-disc test results (see Table 8), in which the SWR for HCCI+20 %Al<sub>2</sub>O<sub>3</sub> was

**Table 9**

Specific wear rates (SWR) of the HCCI clad, HCCI (HP), HCCI+20 %Al<sub>2</sub>O<sub>3</sub> and HCCI+20 %ZTA from the Taber linear abrasion test.

Material	SWR (mm <sup>3</sup> /Nm)
HCCI clad	$4.27 \times 10^{-7}$
HCCI (HP)	$5.03 \times 10^{-5}$
HCCI/20Al <sub>2</sub> O <sub>3</sub>	$5.74 \times 10^{-8}$
HCCI/20ZTA	$1.21 \times 10^{-5}$

the highest.

As already mentioned, the contact stresses between the material surface and the counterspecimen in the Taber linear abrasion test are lower than in the ball-on-disc test. In the ball-on-disc test, a 6 mm hard sapphire ball was utilized, where the local pressure, at least in the initial stage is, according to the Hertz model, several orders of magnitude higher than in the Taber abrasion test, which employed a flat-end pin of 6.35 mm in diameter made of sintered SiC and SiO<sub>2</sub> manifesting sharp edges (see Fig. 20a). This may result in microcracking at the alumina/matrix interfaces, thereby facilitating the pullout of the alumina particles and increasing the material loss rate in the ball-on-disc test (see Table 8). In contrast, the Taber test utilizes a significantly larger contact area of the flat-end cylindrical pin and a lower contact stress. Consequently, there is a suppressed tendency of microcracking and particle pullout.

The wear traces in Fig. 21a–d show surface plowing by the hard particles of the counterspecimen, suggesting an abrasive wear mechanism. It should be noted that in the Taber tests, the wear response of the material is more "global" than in ball-on-disc tests. Fig. 21a shows the worn surface of the HCCI clad. Due to the higher hardness of counterspecimen material and its microstructure, a significant amount of debris is visible with plastic deformation marks across the wear line. This is similar to the three-body wear process that results in material loss. However, the high homogeneity and lack of porosity due to the cladding process results in good wear properties in the Taber test. The hot-pressed HCCI (HP) specimen (Fig. 21b) is characterized by numerous grooves and delamination areas, which is directly reflected in the high SWR value (Table 9). As evidenced in Fig. 21c (see also

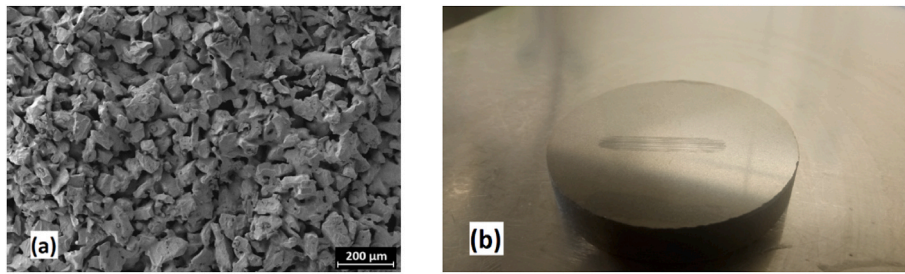


**Fig. 20.** (a) SEM image of counterspecimen used in the Taber linear abrasive wear test; (b) macroscopic image of HCCI+20 %Al<sub>2</sub>O<sub>3</sub> composite specimen after the Taber wear test.

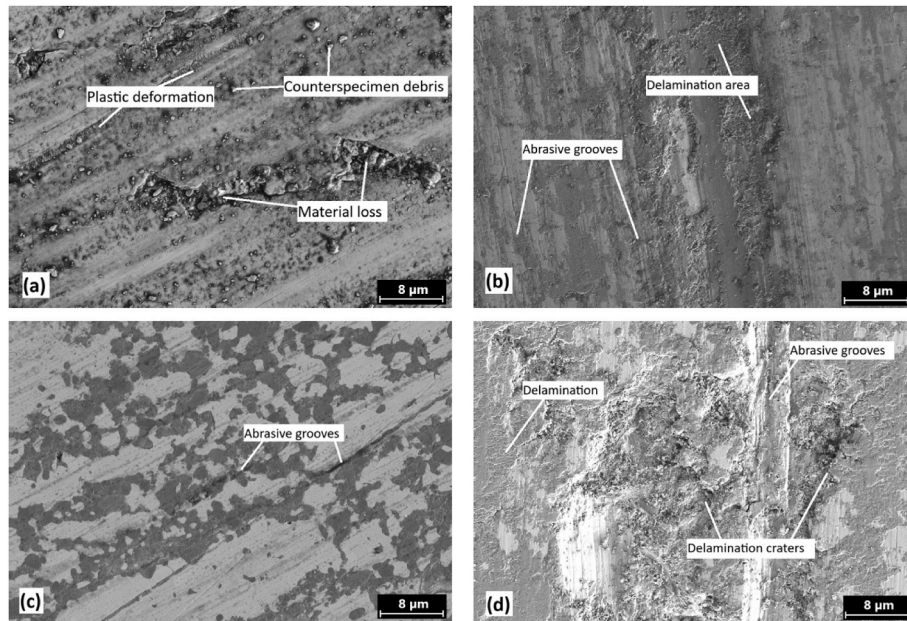


**Fig. 21.** SEM micrographs of worn surfaces after linear abrasion test using Taber 5750 device: (a) HCCI clad, (b) HCCI (HP), (c) HCCI+20 %Al<sub>2</sub>O<sub>3</sub>, (d) HCCI+20 %ZTA.

Fig. 20b), the HCCI+20 %Al<sub>2</sub>O<sub>3</sub> composite demonstrates a significantly lower degree of abrasive wear when compared to the HCCI clad material (Fig. 21a). The abrasion grooves are also visible, but they are significantly smaller, and the plowing traces are least pronounced in HCCI+20 %Al<sub>2</sub>O<sub>3</sub> composite. Tearing off of small ceramic particles can be detected, which can be defined as the main mechanism responsible for the mass loss. The presence of locally torn particles is evident, yet the overall degree of material loss is minimal for the HCCI+20 %Al<sub>2</sub>O<sub>3</sub> composite. In the case of HCCI+20 %ZTA (Fig. 21d), the lower material's relative density (95.1 %) and lower hardness (see Table 4) result in

the higher mass loss. Here, a complex wear mechanism is observed with delamination craters along with plowing and tearing off of the ceramic particles, creating sharp edges that also accelerate the mass loss of the counterspecimen. The three-body abrasive wear-like mechanisms, in conjunction with the low density, result in the greatest material loss among the materials that were tested.

As already mentioned, the Taber linear abrasive wear test provides a more comprehensive evaluation of the wear behavior of the materials studied in regard of their application to ball mills. In this context, the relatively high porosity of the HCCI+20 %ZTA composite

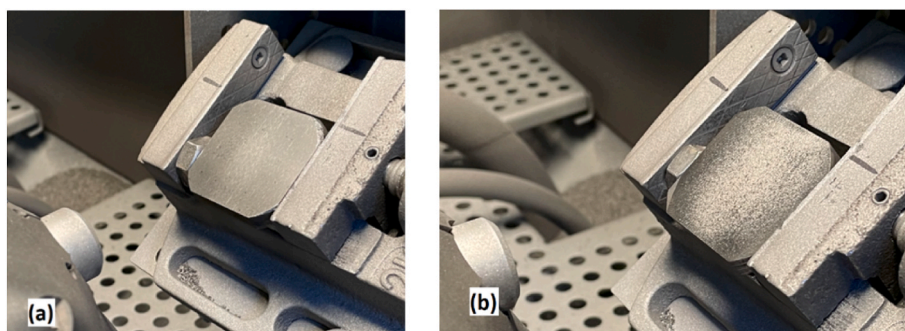


**Fig. 22.** View of a test specimen (30) HCCI+20Al<sub>2</sub>O<sub>3</sub> before (a), and after the abrasive blasting wear test (b).

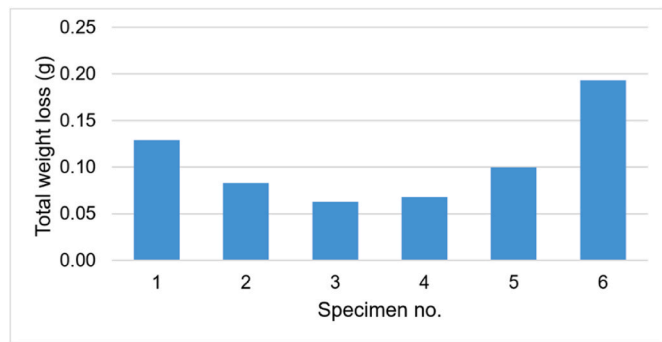


Fig. 23. Total weight loss in the abrasive blasting wear test. Specimens labels: 1. (30)HCCI clad, 2. (70)HCCI clad, 3. (30)HCCI+20 %Al<sub>2</sub>O<sub>3</sub>, 4. (70)HCCI+20 %Al<sub>2</sub>O<sub>3</sub>, 5. (30)HCCI+20 %ZTA, 6. (70)HCCI+20 %ZTA.

(approximately 5 %) plays a significant role in its poor wear performance in the Taber test. The geometry of the flat pin further amplifies the mass loss effect. Consequently, the combined factors of high porosity and the flat pin geometry contribute to the higher mass loss of HCCI+20 %ZTA composite when compared to the performance of this material in the ball-on-disc test.

3.2.3.3. Abrasive blasting wear test. The enhanced wear resistance of HCCI+20 %Al<sub>2</sub>O<sub>3</sub> composite is further substantiated by the results of the

abrasive blasting test, which are reported below for two angles of incidence of the abrasive jet to the sample surface, 30° and 70°. These two angles are reflected in the notation used below by adding (30) or (70), in front of the material composition, respectively. An example of a specimen view before and after the abrasive blasting test is shown in Fig. 22. The area of impact of the abrasive blasting stream on the tested surfaces is clearly visible.

The surface wear was determined by the weight loss measurements and the results for the investigated materials are shown in Fig. 23 and Table 10.

The data in Fig. 23 show that the total weight loss recorded for the HCCI+20 %Al<sub>2</sub>O<sub>3</sub> composite is the lowest for both angles of incidence of the abrasive jet, 30° and 70°. In other words, the HCCI+20 %Al<sub>2</sub>O<sub>3</sub> composite has a significantly higher resistance to abrasive blast wear than the HCCI clad and HCCI+20 %ZTA as shown in the last column of Table 10. In addition, it can be seen from Table 10 that the HCCI+20 %ZTA specimen shows approximately constant level of wear over time, while the other specimens show the highest wear during the first 10 s of the test, with the wear decreasing in the following stages. This may indicate that a more wear resistant surface layer is formed on the HCCI clad and HCCI+20 %Al<sub>2</sub>O<sub>3</sub> specimens.

The SEM images in Fig. 24 show the surface after abrasive blasting. This is one of the most aggressive surface treatment methods involving the use of loose abrasive media with high kinetic energy, which apart from removing the surface material leads to deformation and development of the treated surface. When a solid sharp-edged hard particle impinges on a material surface, it may skid and/or rotate on the surface,

Table 10

Results of the abrasive blasting wear test obtained for the composite material HCCI+20 %Al<sub>2</sub>O<sub>3</sub> with (30), (70) denoting the angles of incidence of the abrasive jet to the sample surface. The data shows that the (30)HCCI+20 %Al<sub>2</sub>O<sub>3</sub> material has the highest, while the (70)HCCI+20 %Al<sub>2</sub>O<sub>3</sub> material has the second highest resistance to abrasive blasting.

Material	Specimen	Loss of weight after the next machining cycle						Total weight loss (g)	Relative abrasion resistance
		10 s	20 s	30 s	40 s	50 s	60 s		
(30)HCCI clad	1	0.063	0.034	0.01	0.008	0.008	0.006	0.129	0.49
(70)HCCI clad	2	0.023	0.019	0.008	0.012	0.011	0.010	0.083	0.76
(30)HCCI+20 %Al <sub>2</sub> O <sub>3</sub>	3	0.015	0.019	0.004	0.009	0.011	0.005	0.063	1
(70)HCCI+20 %Al <sub>2</sub> O <sub>3</sub>	4	0.019	0.01	0.010	0.009	0.009	0.011	0.068	0.93
(30)HCCI+20 %ZTA	5	0.009	0.021	0.016	0.018	0.017	0.019	0.100	0.63
(70)HCCI+20 %ZTA	6	0.031	0.035	0.031	0.032	0.030	0.034	0.193	0.33

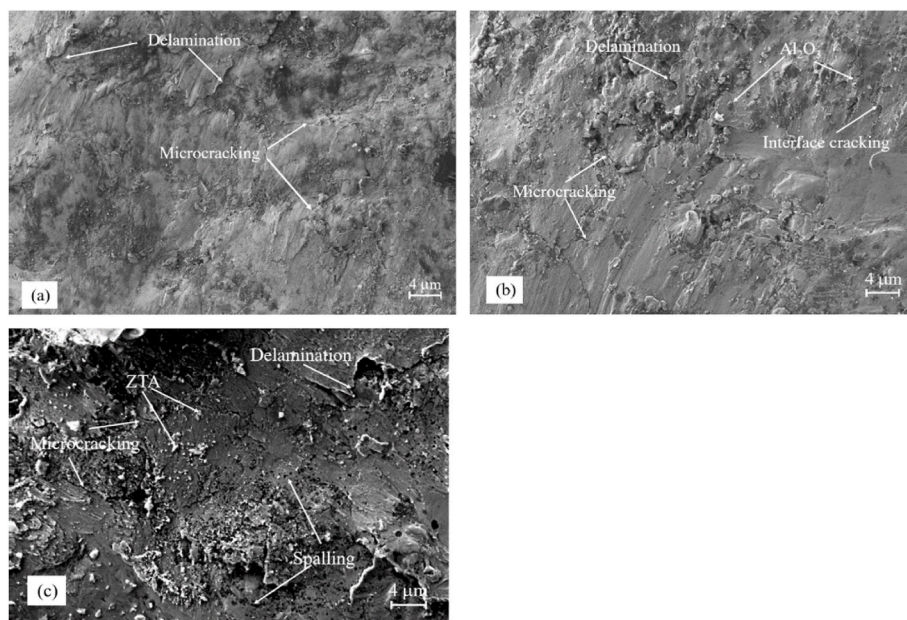


Fig. 24. SEM images of worn surfaces after abrasive blasting wear test: (a) HCCI clad, (b) HCCI+20 %Al<sub>2</sub>O<sub>3</sub> composite, (c) HCCI+20 %ZTA composite.

and at the same time create an indentation (ductile materials) or crater (brittle materials). With successive impacts of particles on the same location, this indentation causes material removal due to the repeated plastic deformation and the skidding of sharp-edged hard particles over a surface of relatively lower hardness. If the abrasive particle impact below critical speed in relatively hard surface the particle does not skid but rotate, resulting in no intensive cutting damage but more likely plastic fatigue damage.

The surface images in Figs. 24a and b differ slightly in terms of wear intensity, while the surface in Fig. 24c is clearly more developed with a relatively large share of craters and inhomogeneities. This is evident from the results in Table 10, where the highest observed wear is for the HCCI+20 %ZTA specimens. In the HCCI clad sample (Fig. 24a), delamination and microcracking can be observed on the surface. In the HCCI+20 %Al<sub>2</sub>O<sub>3</sub> sample (Fig. 24b), in addition to delaminations and microcracks, some microcracks also appear at the interface between the HCCI matrix and the alumina grains. It was already mentioned that the HCCI+20 %ZTA specimen (Fig. 24c) shows many craters left by the ZTA grains that were torn out during the test. This mechanism is mainly responsible for the wear of this material during abrasive blasting. The wear mechanisms depicted in Fig. 24 have also been reported by other authors for iron based materials under impact abrasive wear conditions [41].

#### 4. Conclusions

This study presents a promising approach to utilize industrial waste by developing a high-performance composite material through the integration of high-chromium cast iron (HCCI) shavings with commercial electrocorundum (Al<sub>2</sub>O<sub>3</sub>). The key findings and implications are summarized below.

- Through optimization of the high-energy ball milling and hot pressing processes, an HCCI+20 %Al<sub>2</sub>O<sub>3</sub> composite with a remarkably high relative density (99.84 %) was successfully obtained.
- This composite exhibits (i) satisfactory fracture toughness both in static and dynamic cases, (ii) enhanced hardness, and (iii) excellent wear resistance in the Taber linear abrasion test and the abrasive blasting test.
- From an industrial perspective, the HCCI+20 %Al<sub>2</sub>O<sub>3</sub> composite is noteworthy for two reasons: (i) the waste HCCI shavings and commercial electrocorundum powder are low-cost materials, (ii) the composite is machinable, which is an asset in industrial production.
- The hot pressing technique used to consolidate the HCCI+20 %Al<sub>2</sub>O<sub>3</sub> composite has several advantages over casting methods. However, the process time and total energy cost may pose challenges to the commercialization of this material.

#### Declaration of funding

The authors declare no funding or research grants (and their source) received in the course of study, research or assembly of the manuscript.

#### Declaration of competing interest

The authors declare that they have no known competing financial interests or personal relationships that could have appeared to influence the work reported in this paper.

#### Acknowledgement

The authors would like to thank Mr. Sławomir Sroczyński and Mr. Artur Merchut of FPM S.A. (Mikołów, Poland) for providing the HCCI material and for their valuable cooperation in the early stages of this research.

#### Appendix A. Supplementary data

Supplementary data to this article can be found online at <https://doi.org/10.1016/j.jmrt.2025.06.109>.

#### References

- [1] Wang S, Liao X, Zheng Z, Long J, Shen M, Chen W, et al. Exploring the hardness-independent wear behavior of typical wear-resistant materials under dynamic and static conditions. *J Mater Res Technol* 2024;33:6798. <https://doi.org/10.1016/j.wear.2022.204489>. 09.
- [2] Pareek P, Sankhla VS. Review on vertical roller mill in cement industry & its performance parameters. *Mater Today Proc* 2021;44:4621–7. <https://doi.org/10.1016/j.matpr.2020.10.916>.
- [3] Holmberg K, Kivikytö-Reponen P, Härkisaari P, Valtonen K, Erdemir A. Global energy consumption due to friction and wear in the mining industry. *Tribol Int* 2017;15:116–39. <https://doi.org/10.1016/j.triboint.2017.05.010>.
- [4] Nejad RM, Shariati M, Farhangdoost K. Effect of wear on rolling contact fatigue crack growth in rails. *Tribol Int* 2016;94:118–25. <https://doi.org/10.1016/j.triboint.2017.05.010>.
- [5] Nieminen R, Autio J, Suomalainen E, Husu N, Kauppi M, Väänänen E. Wear mechanism of Ni-Hard4 rollers in chromite ore crushing. *Wear* 1994;179:95–100. [https://doi.org/10.1016/0043-1648\(94\)90225-9](https://doi.org/10.1016/0043-1648(94)90225-9).
- [6] Jensen LRD, Fundal E, Møller P, Jespersen M. Wear mechanism of abrasion resistant wear parts in raw material vertical roller mills. *Wear* 2011;271:2707–19. <https://doi.org/10.1016/j.wear.2011.03.018>.
- [7] Mohammadnezhad M, Javaheri V, Shamanian M, Naseri M, Bahrami M. Effects of vanadium addition on microstructure, mechanical properties and wear resistance of Ni-Hard4 white cast iron. *Mater Des* 2013;49:888–93. <https://doi.org/10.1016/j.matdes.2013.02.043>.
- [8] Ngqase M, Pan X. An overview on types of white cast irons and high chromium white cast irons. *J Phys: Conf Series* 2020;1495:012023. <https://doi.org/10.1088/1742-6596/1495/1/012023>.
- [9] Feng A, Wei Y, Liu B, Chen Ch, Pan X, Xue J. Microstructure and mechanical properties of composite strengthened high-chromium cast iron by laser quenching and laser shock peening. *J Mater Res Technol* 2022;20:4342–55. <https://doi.org/10.1016/j.jmrt.2022.08.148>.
- [10] Pagounis E, Lindroos VK. Processing and properties of particulate reinforced steel matrix composites. *Mat Sci Eng A* 1998;246:221–34. [https://doi.org/10.1016/S0921-5093\(97\)00710-7](https://doi.org/10.1016/S0921-5093(97)00710-7).
- [11] Zum Gahr K. Wear by hard particles. *Tribol Int* 1999;31:587–96. [https://doi.org/10.1016/S0301-679X\(98\)00079-6](https://doi.org/10.1016/S0301-679X(98)00079-6).
- [12] Zheng K, Gao Y, Li Y, Zhao S, Wang J. Three-body abrasive wear resistance of iron matrix composites reinforced with ceramic particles. *Proc Inst Mech Eng Part J J Eng Tribol* 2014;228:3–10. <https://doi.org/10.1177/1350650113496700>.
- [13] Li Z, Jiang Y, Zhou R, Lu D, Zhou R. Dry three-body abrasive wear behavior of WC reinforced iron matrix surface composites produced by V-EPC infiltration casting process. *Wear* 2007;262:649–54. <https://doi.org/10.1016/j.wear.2006.07.009>.
- [14] Ru J, He H, Jiang Y, Zhou R, Hua Y. Wettability and interaction mechanism for Ni-modified ZTA particles reinforced iron matrix composites. *J Alloys Compd* 2019;786:321–9. <https://doi.org/10.1016/j.jallcom.2019.01.342>.
- [15] Qiu B, Xing S, Dong Q, Liu H. Comparison of properties and impact abrasive wear performance of ZrO<sub>2</sub>-Al<sub>2</sub>O<sub>3</sub>/Fe composite prepared by pressure casting and infiltration casting process. *Tribol Int* 2020;142:105979. <https://doi.org/10.1016/j.triboint.2019.105979>.
- [16] Wang Y, Qin Y, Zou X, Chen H. Formation mechanism of interface layer of ZTA particle reinforced iron matrix composite. *J Mater Res Technol* 2024;32:1565–76. <https://doi.org/10.1016/j.jmrt.2024.08.016>.
- [17] Ru J, Jiang Y, Zhou R, Feng J, Hua Y, Yang Q. Preparation of Ni-encapsulated ZTA particles as precursors to reinforce iron-based composites. *Adv Eng Mater* 2017;19:1–11. <https://doi.org/10.1002/adem.201700268>.
- [18] Bahraini M, Minghetti T, Zoellig M, Schubert J, Bertho K, Schelle C, et al. Activated pressureless infiltration of metal-matrix composites with graded activator content. *Comp Part A* 2009;40:1566–72. <https://doi.org/10.1016/j.compositesa.2009.06.016>.
- [19] Vasic S, Grobety B, Kuebler J, Kern P, Graule T. Experimental models for activation mechanism of pressureless infiltration in the non-wetting steel-alumina MMC-system. *Adv Eng Mater* 2008;10:471–5. <https://doi.org/10.1002/ADEM.200700342>.
- [20] Li Y, Li C, Tang S, Zheng Q, Wang J, Zhang Z, et al. Interfacial bonding and abrasive wear behavior of iron matrix composite reinforced by ceramic particles. *Materials* 2019;12:3646. <https://doi.org/10.3390/ma12223646>.
- [21] Li C, Li Y, Shi J, Li B, Gao Y, Goei R, et al. Interfacial characterization and erosive wear performance of zirconia toughened alumina ceramics particles reinforced high chromium white cast irons composites. *Tribol Int* 2022;165:107262. <https://doi.org/10.1016/j.triboint.2021.09.214>.
- [22] Maj J, Węglewski W, Bochenek K, Rogal Ł, Woźniacka S, Basista M. A Comparative study of mechanical properties, thermal conductivity, residual stresses, and wear resistance of aluminum-alumina composites obtained by squeeze casting and powder metallurgy. *Metall Mater Trans A* 2021;52:4727–36. <https://doi.org/10.1007/s11661-021-06401-7>.
- [23] Tang SL, Gao YM, Li YF. Recent developments in fabrication of ceramic particle reinforced iron matrix wear resistant surface composite using infiltration casting

- technology. *Ironmak Steelmak* 2014;41:633–40. <https://doi.org/10.1179/1743281213Y.0000000175>.
- [24] Qiu B, Xing S, Dong Q. Fabrication and wear behavior of ZTA particles reinforced iron matrix composite produced by flow mixing and pressure compositing. *Wear* 2019;428–429:167–77.
- [25] Fang Y, Kim M-K, Zhang Y, Duan Z, Yuan Q, Suhr J. Particulate-reinforced iron-based metal matrix composites fabricated by selective laser melting: a systematic review. *J Manuf Process* 2022;74:592–639. <https://doi.org/10.1016/j.jmapro.2021.12.018>.
- [26] Zhou D, Qiu F, Wang H, Jiang Q. Manufacture of nano-sized particle-reinforced metal matrix Composites: a Review. *Acta Metall Sin (Engl Lett)* 2014;27:798–805. <https://doi.org/10.1007/s40195-014-0154-z>.
- [27] ISO 23146 Advanced Technical Ceramics - Test methods for fracture toughness of monolithic ceramics - Single-edge V-notch beam (SEVNB) method, 2015.
- [28] ISO 12737 Metallic Materials - Determination of plane-strain fracture toughness, 2011.
- [29] ISO 26843 Metallic materials – Measurement of fracture toughness at impact loading rates using pre-cracked Charpy type test pieces, 2015.
- [30] Qin Y, Wang Y, Miao W, Yang P, Fu D, Fan L, et al. Interface modification and impact abrasive wear behavior of ZTA particle-reinforced iron-matrix composite. *Wear* 2022;490–491:204205. <https://doi.org/10.1016/j.wear.2021.204205>.
- [31] Rajendhran N, Pondicherry K, Huang S, Vleugels J, De Baets P. Influence of abrasive characteristics on the wear micro-mechanisms of NbC and WC cermets during three-body abrasion. *Wear* 2023;530–531:205007. <https://doi.org/10.1016/j.wear.2023.205007>.
- [32] Jurci P, Dlouhy I. Cryogenic treatment of martensitic steels: microstructural fundamentals and implications for mechanical properties and wear and corrosion performance. *Materials* 2024;17:48.
- [33] Sobotová J, Jurci P, Dlouhy I. The effect of sub-zero treatment on microstructure, fracture toughness, and wear resistance of Vanadis 6 tool steel. *Mater Sci Eng, A* 2016;652:192–204. <https://doi.org/10.1016/j.msea.2015.11.078>.
- [34] Zheng B, Huang Z, Xing J, Fan X. Three-body abrasive wear behavior of cementite with different chromium concentrations. *Tribol Lett* 2016;61:13. <https://doi.org/10.1007/s11249-015-0632-0>.
- [35] Wang L, Niinomi M, Takahashi S, Hagiwara M, Emura S, Kawabe Y, et al. Relationship between fracture toughness and microstructure of Ti–6Al–2Sn–4Zr–2Mo alloy reinforced with TiB particles. *Mat Sci Eng A* 1999;263:319–25. [https://doi.org/10.1016/S0921-5093\(98\)01163-0](https://doi.org/10.1016/S0921-5093(98)01163-0).
- [36] Kumar M, Megalingam A. Tribological characterization of Al6061/alumina/graphite/redmud hybrid composite for brake rotor application. *Part Sci Technol* 2014;37:261–74. <https://doi.org/10.1080/02726351.2017.1367747>.
- [37] Moore MA. The relationship between the abrasive wear resistance, hardness and microstructure of ferritic materials. *Wear* 1974;28:59–68.
- [38] Bembalge OB, Panigrahi SK. Influence of SiC ceramic reinforcement size in establishing wear mechanisms and wear maps of ultrafine grained AA6063 composites. *Ceram Int* 2019;45:20091–104. [https://doi.org/10.1016/0043-1648\(74\)90101-X](https://doi.org/10.1016/0043-1648(74)90101-X).
- [39] Joshi TC, Rathore SS, Dabhade VV, Prakash U. Dry sliding wear behavior of sinter forged micrometric and nanometric yttrium oxide reinforced AA-7075 matrix composites. *J Alloys Metall Systems* 2024;6:100067. <https://doi.org/10.1016/j.jalmes.2024.100067>.
- [40] Gupta PD, Kumar D, Parkash O, Jha AK, Sadasivuni KK. Dependence of wear behavior on sintering mechanism for iron-alumina metal matrix nanocomposites. *Mater Chem Phys* 2018;220:441–8. <https://doi.org/10.1016/j.matchemphys.2018.08.079>.
- [41] Wang Y, Qin Y, Fu D, Chen H, Pan Y, Zhu C, et al. Behaviors of ZTA (zirconia toughened alumina) reinforced iron composites under impact abrasive wear conditions. *Wear* 2020;458–459:203397. <https://doi.org/10.1016/j.wear.2020.203397>.